ELSEVIER

Available online at www.sciencedirect.com
ScienceDirect

Theoretical Population Biology 72 (2007) 274–291

Theoretical Population Biology

www.elsevier.com/locate/tpb

Epidemiological effects of seasonal oscillations in birth rates

Daihai He*, David J.D. Earn

Department of Mathematics and Statistics, McMaster University, Hamilton, Ont., Canada L8S 4K1

Received 26 October 2006
Available online 7 May 2007

Abstract

Seasonal oscillations in birth rates are ubiquitous in human populations. These oscillations might play an important role in infectious disease dynamics because they induce seasonal variation in the number of susceptible individuals that enter populations. We incorporate seasonality of birth rate into the standard, deterministic susceptible–infectious–recovered (SIR) and susceptible–exposed–infectious–recovered (SEIR) epidemic models and identify parameter regions in which birth seasonality can be expected to have observable epidemiological effects. The SIR and SEIR models yield similar results if the infectious period in the SIR model is compared with the "infected period" (the sum of the latent and infectious periods) in the SEIR model. For extremely transmissible pathogens, large amplitude birth seasonality can induce resonant oscillations in disease incidence, bifurcations to stable multi-year epidemic cycles, and hysteresis. Typical childhood infectious diseases are not sufficiently transmissible for their asymptotic dynamics to be likely to exhibit such behaviour. However, we show that fold and period-doubling bifurcations generically occur within regions of parameter space where transients are phase-locked onto cycles resembling the limit cycles beyond the bifurcations, and that these phase-locking regions extend to arbitrarily small amplitude of seasonality of birth rates. Consequently, significant epidemiological effects of birth seasonality may occur in practice in the form of transient dynamics that are sustained by demographic stochasticity.

Keywords: Resonance; Scaling; Bifurcations; Hysteresis

1. Introduction

Communicable disease surveillance over the last century has produced many valuable time series that reveal the temporal and spatial epidemic patterns caused by a wide variety of pathogens (Anderson and May, 1991; Grenfell and Harwood, 1997; Earn et al., 1998, 2002; Grenfell et al., 2001). These time series have stimulated the development and analysis of numerous mathematical models of infectious disease transmission, which aim to identify the mechanisms that generate observed epidemic patterns and to design strategies for control and eradication (Kermack and McKendrick, 1927; Bartlett, 1960; Bailey, 1975; Anderson and May, 1991).

Until the 1970s, the mathematical theory of infectious diseases was focused on autonomous deterministic and stochastic models. London and Yorke (1973) recognized that the contact rate among individuals is not constant but varies seasonally as a result of the aggregation of children in schools. Hence, the disease transmission rate is subject to exogenous seasonal forcing, making the system non-autonomous and leading potentially to complex dynamics. Indeed, subsequent studies established that seasonal forcing of the transmission rate can lead to multiple coexisting stable cycles (Schwartz and Smith, 1983) and chaos (Olsen and Schaffer, 1990; Glendinning and Perry, 1997). Recent work has shown that a suitably parameterized, seasonally forced transmission model can successfully predict observed transitions in the temporal structure of epidemics for a variety of childhood infectious diseases, based on slow changes in vaccination levels and birth rates (Earn et al., 2000; Bauch and Earn, 2003).

In addition to the secular changes that occur over decades, it is well known that birth rates oscillate seasonally, and this has been implicated in the incidence

---

*Corresponding author. Department of Ecology and Evolutionary Biology, University of Michigan, 2056/2060 Kraus Natural Science Bldg., 830 North University Ave., Ann Arbor, MI 48109, USA.
Fax: +1 734 763 0544.
E-mail addresses: daihai@umich.edu (D. He), earn@math.mcmaster.ca (D.J.D. Earn).

0040-5809/$ - see front matter © 2007 Elsevier Inc. All rights reserved.
doi:10.1016/j.tpb.2007.04.004

patterns of some non-communicable diseases such as schizophrenia and diabetes (Miura, 1987). From the point of view of infectious diseases, birth rate seasonality represents an additional source of exogenous seasonal forcing. In this paper, we investigate how seasonal oscillation in birth rates influences the dynamics of the simplest standard models of childhood infectious disease transmission (the susceptible–infectious–recovered or SIR model and the susceptible–exposed–infectious–recovered or SEIR model). We begin with a brief discussion of some birth data showing seasonal oscillations, from which we estimate the magnitude of seasonal forcing of birth rates. We then review the dynamics of the basic SIR model before exploring the theoretical consequences of birth rate seasonality.

2. Data showing seasonality of birth rates

Seasonality of birth rate has been observed in almost all historical populations (Trovato and Odynak, 1993). Two distinct patterns are evident in modern populations: the *American pattern* with a trough in April–May and a peak in September, and the *European pattern* with a peak in spring–summer and a secondary peak in September (Trovato and Odynak, 1993; Doblhammer et al., 2000; Haandrikman, 2003). In spite of its proximity to the United States, Canada's pattern of births since the early 1900s has been similar to that of Europe (Trovato and Odynak, 1993).

Figs. 1a and 2a show monthly births in Canada and the US for 10 yr from 1991 to 2000. Both secular trends and seasonal oscillations are evident in these two time series. To quantify the amplitude of seasonal variation, we must remove the trends, which we do as follows.

We denote the raw monthly data, i.e., the number of births in month j of year i, by X_{ij}. The average number of births in a month of average length in year i is

$$\langle X\rangle_i = \frac{1}{12}\sum_{j=1}^{12} X_{ij}. \tag{1}$$

To correct for the different lengths of each month we define

$$c_{ij} = \frac{(\text{Days in year } i)/12}{\text{Days in month } j \text{ of year } i}. \tag{2}$$

The scaled, month-length-corrected monthly data is then

$$Y_{ij} = \frac{c_{ij}X_{ij} - \langle X\rangle_i}{\langle X\rangle_i}, \quad i = 1991, \ldots, 2000, \; j = 1, \ldots, 12. \tag{3}$$

In Figs. 1 and 2, the scaled time series defined by Eq. (3) are shown in panel b and their power spectral densities (PSD) are shown in panel c. These examples show that oscillations in birth rates with seasonal amplitude $\varepsilon \sim 0.1$ occur in real populations. For both Canada and the US, the power spectrum has a strong peak at frequency 1 yr^{-1}, reflecting the primarily annual pattern, and a secondary peak at

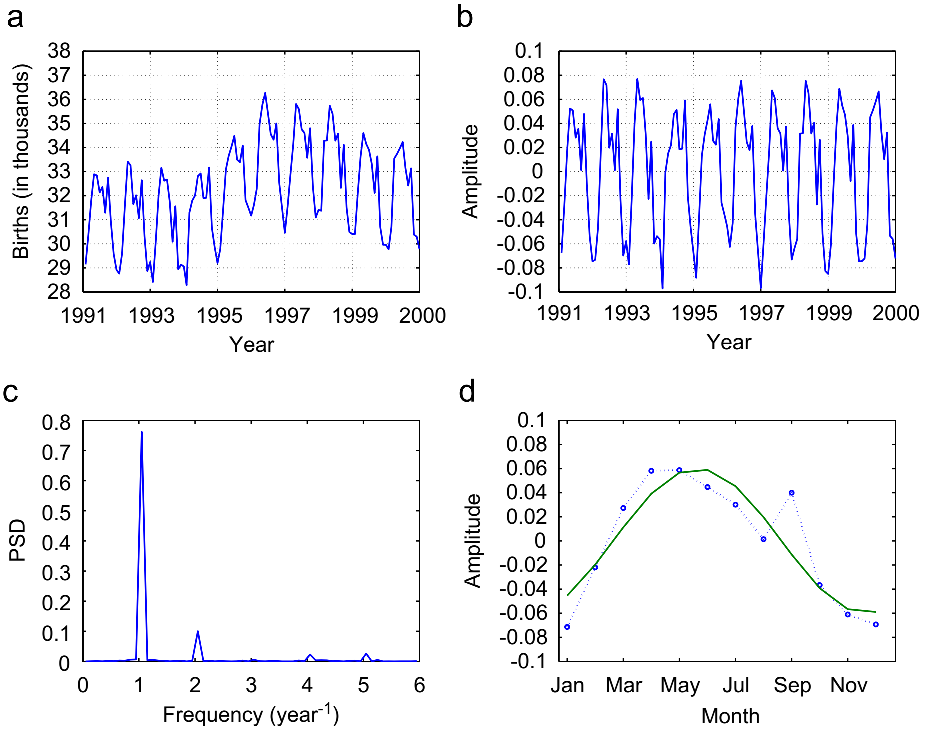

Fig. 1. Monthly births in Canada. The four panels show the raw birth data (a), the scaled, corrected time series defined by Eq. (3) (b), the power spectrum of the scaled time series computed with the FFT routine of Matlab 6 (c), and the average seasonal pattern (d) computed by averaging the scaled data across years (Eq. (4), circles) and fitted with a sine wave (Eq. (5), solid curve). The fitted amplitude of seasonality is $\varepsilon = 0.06$ and the fitted phase shift is $\phi = -0.44\pi$ (i.e., -2.64 months). *Data source*: CANSIM Table 102-4502 available online at `http://www.statcan.ca/` or Table 2.1 of Births, 1991–2000, Statistics Canada (Statistics Canada, Health Statistics Division, 2006).

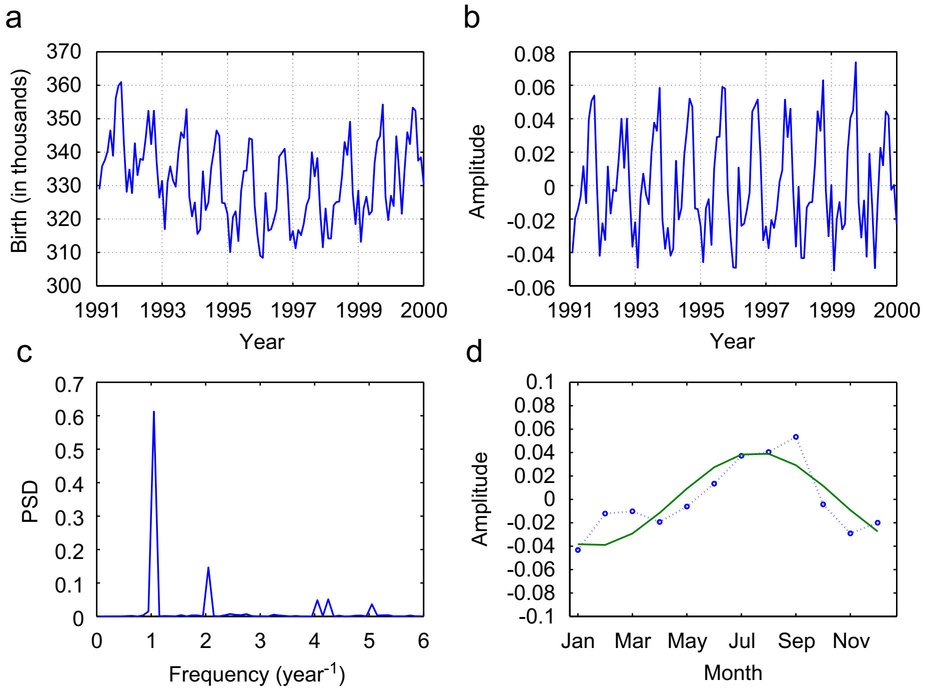

Fig. 2. Monthly births in the US. Panels correspond to those for Canada in Fig. 1. In panel (d), the fitted sine wave has amplitude $\varepsilon = 0.04$ and phase shift $\phi = -0.76\pi$ (-4.56 months, 1.92 months later compared to that of Canada). *Data source*: Annual summary of Monthly Vital Statistics Report, National Center for Health Statistics, United States; `http://www.cdc.gov/nchs/births.htm`.

frequency $2\,\mathrm{yr}^{-1}$ (period $0.5\,\mathrm{yr}$), reflecting the rise in births in September in Canada and May in the US (the spectral peak at $2\,\mathrm{yr}^{-1}$ disappears if we remove the secondary peak in the time series).

On average, the seasonal pattern of births is roughly sinusoidal. Indeed, averaging months across years:

$$Z_j = \frac{1}{N_{\mathrm{yr}}} \sum_{j=1991}^{2000} Y_{ij}, \quad j = 1, \ldots, 12, \tag{4}$$

where $N_{\mathrm{yr}} = 10$, we obtain the average seasonal pattern of births indicated with open circles in panel d of Figs. 1 and 2. The least-squares best fit sine wave through these data is shown as the solid curve. Writing the sine wave,

$$\varepsilon \sin(2\pi t + \phi), \tag{5}$$

the fitted parameters are $(\varepsilon, \phi) = (0.06, -2.64\,\text{months})$ for Canada (Fig. 1) and $(\varepsilon, \phi) = (0.04, -4.56\,\text{months})$ for the US (Fig. 2). The secondary peak in September is evident in Fig. 1d; in the following sections, we ignore this small deviation from sinusoidal oscillation.

3. The standard unforced SIR model

The standard SIR model, originally investigated by Kermack and McKendrick (1927), can be written as

$$\dot{S} = \nu N - \left(\frac{\beta}{N} I + \mu\right) S, \tag{6a}$$

$$\dot{I} = \frac{\beta}{N} IS - (\gamma + \mu) I, \tag{6b}$$

$$\dot{R} = \gamma I - \mu R. \tag{6c}$$

Here, S, I, and R denote the numbers of individuals that are susceptible, infectious, and recovered, respectively, and recovery is assumed to entail lifelong immunity. The total population size is $N = S + I + R$. There are two demographic parameters, the *per capita* birth and natural death rates, which are given by ν and μ, respectively. The epidemiological parameters are the transmission rate β and the recovery rate γ (the mean infectious period is $1/\gamma$). Possible effects of disease-induced mortality are considered in the Appendix.

If we scale the state variables by the population size ($S \to S/N$, $I \to I/N$, $R \to R/N$) and derive equations for these scaled variables (see the Appendix) then we arrive at the simpler system

$$\dot{S} = \nu - (\beta I + \nu) S, \tag{7a}$$

$$\dot{I} = \beta IS - (\gamma + \nu) I, \tag{7b}$$

$$\dot{R} = \gamma I - \nu R, \tag{7c}$$

in which S, I, and R now denote the proportions of the population that are susceptible, infectious, and recovered, respectively. Neither the total population size N nor the natural mortality rate μ appears in these equations. In addition, since $S + I + R = 1$, one of the equations is redundant; henceforth we ignore Eq. (7c).

A fundamental property of an infectious disease is its *basic reproductive ratio* $\mathcal{R}_0$, the mean number of secondary cases caused by a typical primary case in a wholly susceptible population (Anderson and May, 1991). $\mathcal{R}_0$ is the product of the transmission rate, β, and the mean time that an individual is infectious, $1/(\gamma+\nu)$, hence

$$\mathcal{R}_0 = \frac{\beta}{\gamma+\nu}. \tag{8}$$

It is convenient to introduce a second dimensionless parameter

$$\mathcal{G} = \frac{\gamma+\nu}{\nu}, \tag{9}$$

which is the reciprocal of the birth rate expressed as a multiple of the mean time spent in the infectious class. Note that if the population is not changing ($\nu=\mu$) then $\mathcal{G}$ is the mean lifetime in units of the mean time that an individual is infectious. For typical diseases with infectious periods between a few days and a few weeks, $\mathcal{G}$ ranges from $\sim 10^3$ to $\sim 10^4$.

If we measure time in units of the mean infectious period, then Eqs. (7) can be written so they involve only the two dimensionless parameters $\mathcal{R}_0$ and $\mathcal{G}$ (Bauch and Earn, 2004). However, since the mean infectious period γ^{-1} is a more intuitive parameter than $\mathcal{G}$, when displaying results we choose to fix ν and let γ^{-1} vary. No generality is lost in this way; presenting results varying $\mathcal{G}$ would simply involve relabelling axes. The per capita birth rate ν in developed countries in the last century has typically been in the range $0.015 \lesssim \nu \lesssim 0.04\,\mathrm{yr}^{-1}$ (Earn et al., 2000). When presenting results, we always take $\nu = 0.02\,\mathrm{yr}^{-1}$.

The SIR model (7) has at least one and at most two equilibria. For all parameter values, there is a *disease-free equilibrium* (DFE: $S=1, I=0$). The DFE is globally asymptotically stable if $\mathcal{R}_0 \leqslant 1$ and unstable if $\mathcal{R}_0 > 1$. If $\mathcal{R}_0 > 1$ then there is a globally asymptotically stable *endemic equilibrium*

$$\hat{S} = \frac{1}{\mathcal{R}_0}, \tag{10a}$$

$$\hat{I} = \frac{1}{\mathcal{G}}\left(1 - \frac{1}{\mathcal{R}_0}\right). \tag{10b}$$

Global stability analysis of the SIR model is discussed, for example, by Hethcote (2000) (see Korobeinikov and Maini, 2004 for global stability analysis of more general epidemic models). We briefly review the local stability analysis of the endemic equilibrium in order to emphasize aspects that are important to recall when we expand the model to include birth rate seasonality.

We linearize Eqs. (7) by writing $S = \hat{S} + \Delta S$, $I = \hat{I} + \Delta I$ and neglecting quadratic terms ($\Delta S \Delta I$) yielding

$$\begin{pmatrix} \dot{\Delta S} \\ \dot{\Delta I} \end{pmatrix} = \begin{pmatrix} -\nu\mathcal{R}_0 & -\nu\mathcal{G} \\ \nu(\mathcal{R}_0 - 1) & 0 \end{pmatrix} \cdot \begin{pmatrix} \Delta S \\ \Delta I \end{pmatrix}. \tag{11}$$

The eigenvalues of the Jacobian matrix above are

$$\lambda_\pm = -r \pm i\omega, \tag{12a}$$

where

$$r = \nu\mathcal{R}_0/2 \tag{12b}$$

and

$$\omega = \nu\sqrt{\mathcal{G}(\mathcal{R}_0 - 1) - (\mathcal{R}_0/2)^2}. \tag{12c}$$

The approach to the endemic equilibrium will occur via damped oscillations if and only if

$$\mathcal{G} > \mathcal{G}^* = \frac{\mathcal{R}_0^2}{4(\mathcal{R}_0 - 1)}. \tag{13}$$

For typical infections for which the SIR model is reasonable, $\mathcal{G} > 1000$ and $\mathcal{R}_0 \ll 100$, so $\mathcal{G} \gg 25 > \mathcal{G}^*$. Thus, inequality (13) will almost certainly be satisfied and we can expect damped oscillations onto equilibrium (10). The natural frequency of these oscillations is ω and their period is $2\pi/\omega$. In the typical situation in which $\mathcal{G} \gg \mathcal{G}^*$, the second term under the square root in Eq. (12c) can be neglected, so

$$\omega \simeq \nu\sqrt{\mathcal{G}(\mathcal{R}_0 - 1)}. \tag{14}$$

In the vicinity of the endemic equilibrium (10) the solution of the SIR equation (7) is given approximately by the solution of the linearized system (11). Noting that the eigenvectors corresponding to $\lambda_\pm$ in Eq. (12) are $[\lambda_\pm, \nu(\mathcal{R}_0 - 1)]^T$, the general solution of Eq. (11) can be written as

$$\begin{pmatrix} \Delta S(t) \\ \Delta I(t) \end{pmatrix} = e^{-rt}\left\{ c_+ e^{i\omega t}\begin{pmatrix} -r + i\omega \\ \nu(\mathcal{R}_0 - 1) \end{pmatrix} + c_- e^{-i\omega t}\begin{pmatrix} -r - i\omega \\ \nu(\mathcal{R}_0 - 1) \end{pmatrix} \right\}. \tag{15}$$

Here, the constants c_+ and c_- must, necessarily, be complex conjugates, in order to ensure that real initial conditions yield real solutions. Therefore, each component of Eq. (15) has the form $e^{-rt}(z + \bar{z}) = 2e^{-rt}\Re(z)$ and we can write

$$\begin{pmatrix} \Delta S(t) \\ \Delta I(t) \end{pmatrix} = 2e^{-rt}\,\Re\left\{ c_+ e^{i\omega t}\begin{pmatrix} \sqrt{r^2 + \omega^2}\,e^{i\theta} \\ \nu(\mathcal{R}_0 - 1) \end{pmatrix} \right\}, \tag{16}$$

where we have let $\theta = \arctan(-\omega/r)$. It follows that the maximum value of $\Delta S(t)$ is $2e^{-rt}|c_+|\sqrt{r^2+\omega^2}$ and the maximum value of $\Delta I(t)$ is $2e^{-rt}|c_+|\nu(\mathcal{R}_0 - 1)$. We can therefore define the *amplitude of oscillation* in S and I to be

$$\alpha_{S,0} = \frac{(\Delta S)_{\max}}{\hat{S}} \simeq 2e^{-rt}|c_+|\nu\mathcal{R}_0\sqrt{\mathcal{G}(\mathcal{R}_0 - 1)}, \tag{17}$$

$$\alpha_{I,0} = \frac{(\Delta I)_{\max}}{\hat{I}} = 2e^{-rt}|c_+|\nu\mathcal{G}\mathcal{R}_0. \tag{18}$$

These amplitudes decay in time, but their ratio is constant and independent of $|c_+|$. Consequently, independent of initial conditions, we can quantify the shape of the phase portrait near the endemic equilibrium (scaled by the equilibrium values) by the *shape quotient*

$$Q_0 = \frac{\alpha_{I,0}}{\alpha_{S,0}} = \sqrt{\frac{\mathcal{G}}{\mathcal{R}_0 - 1}}. \tag{19}$$

This dimensionless quotient is a measure of the relative amplitudes of oscillation of I and S in the neighbourhood of the endemic equilibrium. Typically $\mathscr{G} > 1000$ and $\mathscr{R}_0 < 25$ so $Q_0 > 6$ (and in general $Q_0 \gg 1$), indicating that the oscillations in I have much greater amplitude than those in S.

4. The SIR model with seasonal oscillation in birth rate

We introduce seasonality of birth rate into the SIR model by replacing every occurrence of v in Eq. (7) with

$$v[1 + \varepsilon \sin(2\pi t/t_{\mathrm{f}} + \phi)]. \tag{20}$$

Here, the amplitude of forcing of the birth rate is $\varepsilon \in [0, 1]$ and period of forcing is

$$t_{\mathrm{f}} = 1\,\mathrm{yr}. \tag{21}$$

The phase shift $\phi \in [0, 2\pi)$ plays no dynamical role; it is included above because it is convenient to associate integer values of t with the start (1 January) of each year when comparing model time series with data.

Our principal goal is to determine whether birth rate seasonality ($\varepsilon > 0$) induces dynamics that are substantially different from the dynamics of the standard SIR model discussed in the previous section. We investigate two ways that qualitatively different dynamics might emerge as ε is increased. First, if the period of natural oscillations happens to coincide with the forcing period t_{f} (1 yr) then the system might exhibit greatly exaggerated oscillations in disease incidence. Such a *resonance* could occur even for extremely weak seasonal forcing, as has been shown in an SIRS influenza model with seasonal forcing of the transmission rate (Dushoff et al., 2004). Second, as ε is increased, bifurcations might be induced, leading to limit cycles of different lengths or more exotic dynamics.

There is no endemic equilibrium if $\varepsilon > 0$. If $0 < \varepsilon \ll 1$ then a limit cycle replaces the equilibrium and we shall see that for typical parameter values limit cycles are the norm for any $\varepsilon \in (0, 1]$. In Eq. (17) for the unforced SIR model ($\varepsilon = 0$) we defined amplitudes of oscillation in S and I during damped oscillations toward the equilibrium; for $\varepsilon > 0$ we focus on the attractor itself, and define the amplitude of oscillation in S and I relative to the average values of S and I on the attractor:

$$\alpha_S = \frac{S_{\max} - \langle S \rangle}{\langle S \rangle}, \quad \alpha_I = \frac{I_{\max} - \langle I \rangle}{\langle I \rangle}, \tag{22}$$

from which we define the *shape quotient*

$$Q_\varepsilon = \frac{\alpha_I}{\alpha_S}. \tag{23}$$

For a given set of parameters and initial conditions, it is straightforward to compute Q_ε: we simply integrate Eqs. (7) numerically until transients have decayed and then compute α_S and α_I defined in Eq. (22), from which we calculate Q_ε via Eq. (23). If multiple attractors coexist then Q_ε will depend on initial conditions (in an example we will describe later in Fig. 5, two distinct annual attractors coexist and have values of Q_ε that differ by 15%).

Note that the shape quotient (23) could be defined in other ways. For example, we have considered defining it in terms of the minimum rather than maximum oscillation amplitudes, or via the difference between maximum and minimum amplitudes rather than their differences from the mean. All these definitions yield qualitatively similar results.

Resonance is indicated if $\alpha_I/\varepsilon \gg 1$, i.e., if oscillations in disease incidence have amplitude many times greater than the externally imposed oscillations in birth rate.

4.1. *Resonance in the limit $\varepsilon \to 0$ (small birth seasonality)*

In the limit $\varepsilon \to 0$ we anticipate that the shape of the limit cycle of the model with birth forcing will be similar to the shape of the transient that approaches the equilibrium in the unforced model. Thus, as $\varepsilon \to 0$ we expect (i) the shape quotient $Q_\varepsilon \to Q_0$, where Q_0 is defined in Eq. (19) and (ii) the frequency of the oscillation should be close to the natural damping frequency ω given in Eq. (12c). Consequently, if ε is sufficiently small then we should be able to identify the parameter values that yield resonance by equating the natural period of damped oscillations of the unforced model ($2\pi/\omega$) with the period of seasonal forcing (t_{f}).

Setting $2\pi/\omega = t_{\mathrm{f}}$ in Eq. (12c), and solving for the *resonant reproductive ratio* $\mathscr{R}_0^*$, we find

$$\mathscr{R}_0^* = 2\mathscr{G} \pm 2\sqrt{\mathscr{G}(\mathscr{G} - 1) - (2\pi/vt_{\mathrm{f}})^2}. \tag{24}$$

If we take the plus sign above we have $\mathscr{R}_0^* > 2\mathscr{G}$, which for typical values of $\mathscr{G}$ (> 1000) yields a resonant reproductive ratio that will never occur in practice. Consequently, we consider only the minus sign in Eq. (24). If $\mathscr{G} \gg \mathscr{G}^*$ (Eq. (13)) then we can approximate ω using Eq. (14), from which setting $2\pi/\omega = t_{\mathrm{f}}$ yields

$$\mathscr{R}_0^* \simeq 1 + \frac{4\pi^2}{v^2 t_{\mathrm{f}}^2 \mathscr{G}} = 1 + \frac{4\pi^2}{v(\gamma + v)t_{\mathrm{f}}^2}. \tag{25}$$

More intuitively, we can express $\mathscr{R}_0^*$ as

$$\mathscr{R}_0^* \simeq 1 + 4\pi^2 \frac{DL}{t_{\mathrm{f}}^2}, \tag{26}$$

where $D = 1/(\gamma + v)$ and $L = 1/v$. If deaths exactly balance births ($\mu = v$) then D is the mean duration of infectiousness and L is the mean lifetime. The line marked "$\varepsilon = 0$" in Fig. 3 shows $\mathscr{R}_0^*$ as a function of $1/\gamma$ for fixed v (which differs negligibly from a plot of $\mathscr{R}_0^*$ as a function D with fixed L).

If we insert expression (24) (using the minus sign) in Eq. (19) we obtain the shape quotient of resonant trajectories in the limit $\varepsilon \to 0$:

$$Q_0^* = \sqrt{\frac{\mathscr{G}}{2\mathscr{G} - 2\sqrt{\mathscr{G}(\mathscr{G} - 1) - (2\pi/vt_{\mathrm{f}})^2} - 1}}. \tag{27}$$

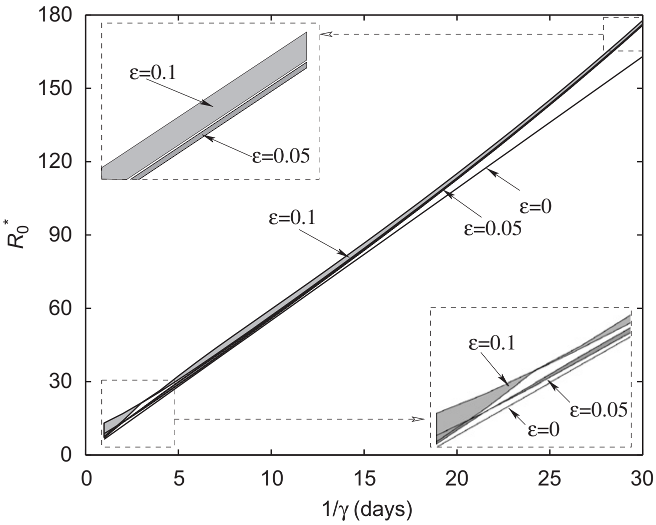

Fig. 3. Resonant reproductive ratios ($\mathscr{R}_0^*$) as function of mean infectious period (γ^{-1}) for fixed average birth rate ($v = 0.02\,\mathrm{yr}^{-1}$) and several amplitudes of birth seasonality ($\varepsilon = 0, 0.05, 0.1$). In the limit $\varepsilon \to 0$, there is a unique resonant reproductive ratio for any specific mean infectious period (Eq. (25) or (26)). For $\varepsilon > 0$, there is a range of resonant reproductive ratios corresponding to any mean infectious period; see Section 4.2.

For typical parameter values, we can instead insert approximation (25) or (26) in Eq. (19) to obtain

$$Q_0^* \simeq \frac{v t_\mathrm{f} \mathscr{G}}{2\pi} = \frac{1}{2\pi}(\gamma + v)t_\mathrm{f} = \frac{t_\mathrm{f}}{2\pi D}. \tag{28}$$

As a concrete example, a mean duration of infection of 13 days yields $D = 0.0356\,\mathrm{yr}$ and a shape quotient at resonance of $Q_0^* \simeq 4.47$.

Fig. 4a shows how the shape quotient depends on mean infectious period (γ^{-1}) in the limit $\varepsilon \to 0$. Using Eq. (19), $Q_0(1/\gamma, \mathscr{R}_0)$ is plotted with dash-dot lines for several fixed values of $\mathscr{R}_0$; the slope of this log–log plot is $-\frac{1}{2}$, as expected from Eq. (19). Using Eq. (27), the resonant shape quotient $Q_0^*(\gamma^{-1})$ is plotted with a heavy solid line; the slope of this log–log plot is -1 over most of the range plotted, as expected from Eq. (28), but bends slightly as the mean infectious period becomes large enough that approximation (28) breaks down and Eq. (27) must be used (with $v = 0.02\,\mathrm{yr}$, the expression under the square root in Eq. (24) becomes negative for $\mathscr{G} \lesssim 314.7$, i.e., for $\gamma^{-1} \gtrsim 58$ days).

Fig. 4d shows phase portraits of three trajectories with little or no birth seasonality: a transient trajectory of the unforced model approaching the equilibrium (light solid curve), a transient trajectory of the forced model with $\varepsilon = 0.0001$ (heavy solid curve), and the limit cycle of the forced model with $\varepsilon = 0.0002$ (dash-dot curve; the value of ε is changed for the limit cycle so it does not overlap the transient). Note that the shape quotient of the unforced and forced transients is different, but that the shape quotient of the limit cycle is similar to its transient.

Figs. 4b and c show how the shape quotient Q_ε (Eq. (23)) depends on γ^{-1} for $\varepsilon = 0.01$ and 0.1, respectively. The dash-dot lines in these panels show $Q_\varepsilon(\gamma^{-1}, \mathscr{R}_0)$ for a wide range of $\mathscr{R}_0$ and there is virtually no dependence on $\mathscr{R}_0$, even for $\varepsilon = 0.1$. Note, moreover, that the slope of these lines is almost identical to the slope of Q_0^* in Fig. 4a. Thus, the resonant shape quotient of the unforced model, given analytically by Eq. (28), is an almost perfect predictor of the shape quotient of limit cycles of the model with modest birth seasonality ($\varepsilon \lesssim 0.1$) whether resonant or not.

This last observation is less surprising if we consider that on any annual limit cycle the condition $2\pi/\omega = t_\mathrm{f}$ must be satisfied, yet this is the only condition that we imposed on the unforced model to derive Eq. (28). To identify resonance ($\alpha_I/\varepsilon \gg 1$) in the forced model, we must impose $2\pi/\omega = t_\mathrm{f}$ not only on the attractor but also on the transient oscillations during the approach to the attractor. While we now see that for small ε the shape of the annual attractor will always be the same, the absolute size of its phase portrait will be much larger at resonance.

4.2. Resonance and hysteresis in the presence of substantial birth seasonality ε

In Section 2 we found that $\varepsilon \sim 0.1$ in practice, so the limit $\varepsilon \to 0$ may not reflect real situations. To estimate the resonant reproductive ratio $\mathscr{R}_0^*$ for $\varepsilon \sim 0.1$, we must resort to numerical computations.

4.2.1. Resonance via numerical analysis of attractors

If we can ignore dependence on initial conditions, then identifying resonance is straightforward (numerically). For given $\mathscr{G}$ (or γ) we can plot α_I/ε as a function of $\mathscr{R}_0$ and identify $\mathscr{R}_0^*$ (the maximum point of the curve). An example of such a plot is shown in Fig. 5a; this example is for $\varepsilon = 0.01$ and Eq. (25) predicts $\mathscr{R}_0^*$ accurately. We note that if $\mathscr{R}_0 = \mathscr{R}_0^*/2$ then the induced oscillations in I have the same amplitude as the imposed oscillations in birth ($\alpha_I/\varepsilon \simeq 1$) and this appears to be true for any infectious period (not just the particular choice of $\gamma^{-1} = 3$ days used in Fig. 5).

We also show α_S/ε and Q_ε in Fig. 5a. The plot of α_S/ε as a function of $\mathscr{R}_0$ confirms that at resonance the oscillations in S are also greatly increased in amplitude, though to a much lesser extent than the oscillations in I (at resonance, $\alpha_S/\varepsilon \simeq 1$ whereas $\alpha_I/\varepsilon \gg 1$). The plot of Q_ε as a function of $\mathscr{R}_0$ confirms that the shape of the phase portrait is almost independent of $\mathscr{R}_0$, with only a slight elongation at resonance.

Fig. 5b examines α_S/ε more closely, for two different amplitudes of birth seasonality ($\varepsilon = 0.01, 0.05$). The solid curve is the same as the thin solid curve in Fig. 5a; it appears identical in shape to the α_I/ε curve in Fig. 5a precisely because the shape quotient Q_ε is nearly constant. A comparison of the solid and dash-dot curves in Fig. 5b reveals that the effect of increasing birth seasonality from $\varepsilon = 0.01$ to 0.05 is to bend the resonance curve to the right, slightly increasing the resonant reproductive ratio $\mathscr{R}_0^*$ (so it is no longer accurately estimated by Eq. (25), which was

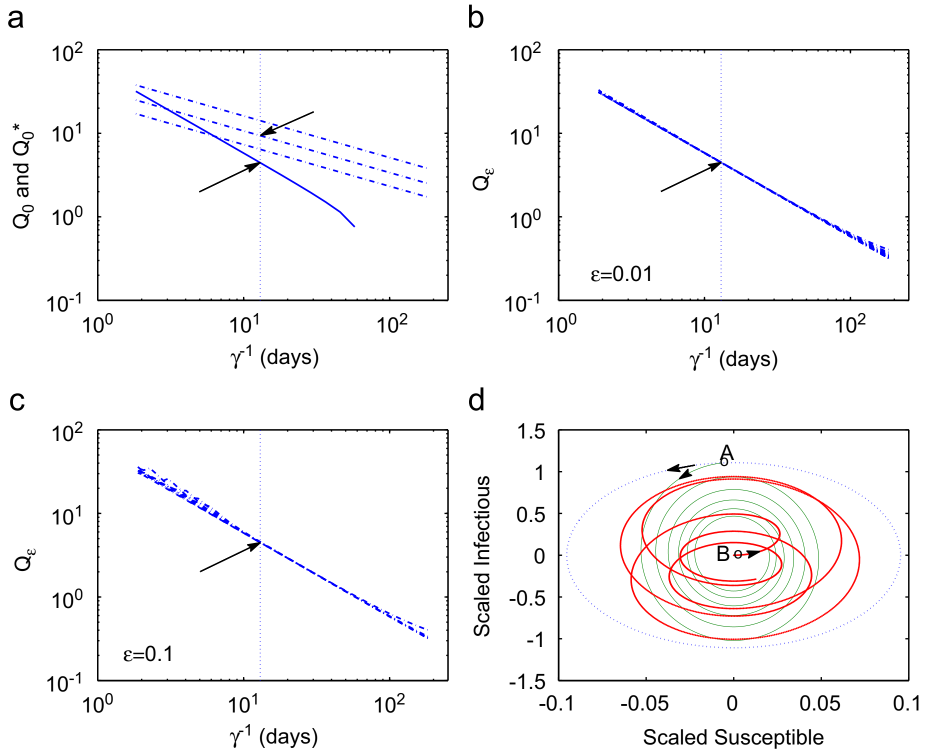

Fig. 4. The shape quotient and resonant shape quotient versus mean infectious period γ^{-1} for the SIR model (7) without seasonal forcing (Q_0, Q_0^*; panel (a)) and with birth rates varying seasonally with amplitude ε (Q_ε, Q_ε^*; panels (b) and (c), and the phase portrait in three situations (panel (d)). The birth rate is $v = 0.02\,\mathrm{yr}^{-1}$ in all plots. In panel (a), dash-dot lines show the shape quotient Q_0 for $\mathscr{R}_0 = 8, 17, 35$ (from top to bottom) based on Eq. (19), while the thick solid line shows Q_0^* as given by Eq. (27); the approximation of Q_0^* given by Eq. (28) is valid until the plotted solid curve begins to bend. In panel (b) for $\varepsilon = 0.01$ and panel (c) for $\varepsilon = 0.1$, dash-dot lines show Q_ε for seven values of the basic reproductive ratio ($\mathscr{R}_0 = 5, 10, 15, \ldots, 35$). Note that although the shape of the attractor (given by Q_ε) is very insensitive to $\mathscr{R}_0$, hence the same whether or not the orbit is resonant, the amplitude of the oscillations will be much larger at resonance. In panels (a)–(c), a vertical dotted line is drawn at $\gamma^{-1} = 13$ days, and the arrow points to the value of Q_0 or Q_ε corresponding to $\mathscr{R}_0 = 17$. Panel (d) shows three phase portraits of the SIR model with $\mathscr{R}_0 = 17$, $\gamma^{-1} = 13$ days, and different degrees of birth seasonality ε. The phase portraits are plotted as $(S(t) - \hat{S})/\hat{S} \times 10^4$ versus $(I(t) - \hat{I})/\hat{I} \times 10^4$, hence the axis labels imply that the amplitude of I is 10 times larger than that of S. The thin solid curve shows the transient trajectory for the unforced SIR model ($\varepsilon = 0$), starting from point A. The thick solid curve shows the transient trajectory with birth seasonality $\varepsilon = 0.0001$, starting from point B (the equilibrium of the unforced model) and continuing for 5 yr. The dotted curve shows the limit cycle for $\varepsilon = 0.0002$.

derived in the limit $\varepsilon \to 0$). (Bending of the graph of $\alpha_I(\mathscr{R}_0)$ to the right has been observed previously in the context of seasonal forcing of the transmission rate β, Greenman et al., 2004; Ireland et al., 2004.)

The effect of increasing the amplitude of birth seasonality further to $\varepsilon = 0.1$ is shown in Fig. 5c. With $\varepsilon = 0.1$, the resonant reproductive ratio is not uniquely defined. In fact, the system appears to exhibit a sort of "memory" for previous values of $\mathscr{R}_0$ (note that both increases or decreases in the effective $\mathscr{R}_0$ over time can occur in practice, for example, as a result of changes in contact rates, Anderson and May, 1991, or vaccination rates, Earn et al., 2000). If we calculate the α_S/ε curve by reducing the reproductive ratio from $\mathscr{R}_0 = 30$ then we obtain the solid curve and conclude $\mathscr{R}_0^* \simeq 20$. Alternatively, if we plot α_S/ε by increasing $\mathscr{R}_0$ from $\mathscr{R}_0 = 5$ then we obtain the dotted curve (also marked with circles) and conclude $\mathscr{R}_0^* \simeq 21$. This is an example of the general phenomenon of *hysteresis*, i.e., dependence of dynamical behaviour on the history of changes in exogenous variables (Macki et al., 1993). Similar phenomena have been identified in other epidemic models near $\mathscr{R}_0 = 1$, where DFE and endemic equilibrium can coexist (Dushoff et al., 1998; van den Driessche and Watmough, 2000).

The hysteresis we observe in Fig. 5c is associated with coexistence of two distinct stable annual cycles. To demonstrate this, we show a bifurcation diagram in Fig. 5d (calculated using CONTENT 1.5, Kuznetsov, 1995). Stable and unstable cycles are indicated by solid and dotted curves, respectively. In the interval $20 \lesssim \mathscr{R}_0 \lesssim 21$, there are two distinct stable annual cycles (with different amplitudes) and one unstable annual cycle. The stable and unstable branches meet at two fold bifurcations. The two coexisting annual attractors have different shape quotients. For example, with $\gamma^{-1} = 3$ days, $\mathscr{R}_0 = 21$, and $\varepsilon = 0.1$, there are two stable annual cycles, one with $Q_\varepsilon = 23$ and the other with $Q_\varepsilon = 26.5$. Their basins of attraction are shown in Fig. 5e.

4.2.2. Resonance via numerical analysis of transients

While the approach adopted to produce Figs.5a–c (analysis of attractors via direct numerical integrations of

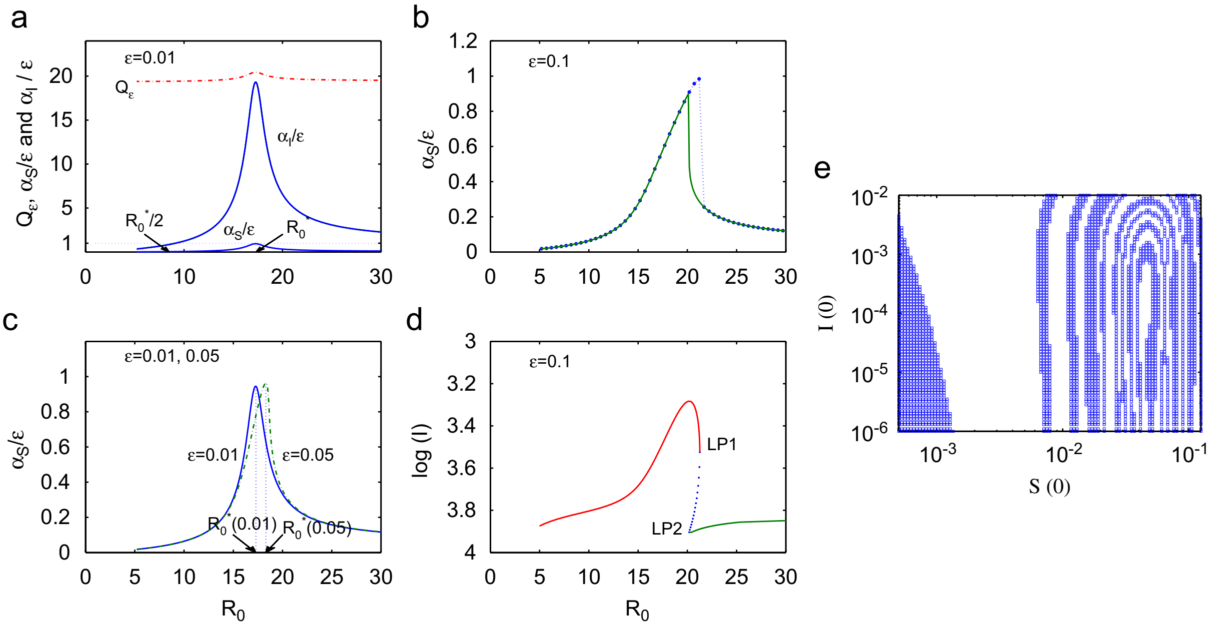

Fig. 5. Identification of resonance and hysteresis in the SIR model (7) with short mean infectious period ($\gamma^{-1} = 3$ days) for several values of the amplitude of birth rate seasonality ($\varepsilon = 0.01, 0.05, 0.1$). Panel (a) (for $\varepsilon = 0.01$) shows, from top to bottom, Q_ε ($= \alpha_I/\alpha_S$), α_I/ε, and α_S/ε as functions of the basic reproductive ratio $\mathscr{R}_0$. $\mathscr{R}_0$ has a negligible effect on the shape quotient Q_ε, but a large effect on the amplitudes of oscillation in S and I. Panel (b) shows that somewhat larger birth seasonality ($\varepsilon = 0.05$) bends the amplitude curves, while panel (c) reveals hysteresis in the presence of more substantial birth seasonality ($\varepsilon = 0.1$). Panel (d) shows a bifurcation diagram (including two fold bifurcations marked LP1 and LP2), which is used in the main text to explain the hysteresis observed in panel (c). Panel (e) shows the basin of attraction of the annual cycle with more elongated shape (larger shape quotient) in the situation where two coexisting annual cycles generate hysteresis.

Eqs. (7)) does identify resonance (and yields an estimate of $\mathscr{R}_0^*$ for a given parameter set), it does not provide any insight as to the origin of the resonance. To *explain* the resonance, we need to examine the transient dynamics, considering the period of damped oscillations onto the attractor. This parallels our approach in the limit $\varepsilon \to 0$ using the unforced SIR model, but we are now without an analytical expression for the frequency ω of damped oscillations. We need to impose the resonance condition $2\pi/\omega = t_{\mathrm{f}}$ using a numerical method.

Fig. 6 shows the result of applying the method described in the next section to calculate ω as a function of $\mathscr{R}_0$ (for a few values of γ^{-1}). Resonant reproductive ratios $\mathscr{R}_0^*$ are values of $\mathscr{R}_0$ for which the period $2\pi/\omega$ is exactly 1 yr. The figure shows that for a given mean infectious period γ^{-1}, resonance occurs over a range of $\mathscr{R}_0$ rather than at a single value of $\mathscr{R}_0$. The heavy solid curves show the period $2\pi/\omega$ in the limit $\varepsilon \to 0$, i.e., given by Eq. (12c). With $\varepsilon = 0.05$ or 0.1, the exact (thin) curves lie above the approximate (thick) curve, over the range of $\mathscr{R}_0$ corresponding to the bend in the peak of the resonance curve in Figs. 5b and c. For $\varepsilon = 0.05$ or 0.1, the curves show *phase-locked* intervals of $\mathscr{R}_0$ rather than a single resonant value of $\mathscr{R}_0$. The curve for $\varepsilon = 0.1$ marked "hysteresis" corresponds to the hysteresis described in relation to Fig. 5c. The inset panel of Fig. 6 shows how the phase-locked range of reproductive ratios varies as a function of amplitude of birth seasonality ε for fixed γ^{-1}. Parameter regions that yield hysteresis are shaded dark grey; phase-locked regions are shaded light grey.

4.3. Numerical calculation of damping frequency ω for general ε

Solutions of the SIR model (7) are pairs of functions $(S(t), I(t))$, defined for all $t \geqslant 0$. Rather than investigating the continuous-time system of differential equations directly, it is convenient to study instead the associated map

$$\mathscr{P}\begin{pmatrix} S(t) \\ I(t) \end{pmatrix} = \begin{pmatrix} S(t+1) \\ I(t+1) \end{pmatrix}. \tag{29}$$

Here, the Poincaré map $\mathscr{P}$ moves the system ahead by exactly 1 yr. For a given initial condition (S_0, I_0) we consider the sequence

$$\begin{pmatrix} S_0 \\ I_0 \end{pmatrix}, \mathscr{P}\begin{pmatrix} S_0 \\ I_0 \end{pmatrix}, \mathscr{P}^2\begin{pmatrix} S_0 \\ I_0 \end{pmatrix}, \ldots, \tag{30}$$

which is equivalent to strobing the original system once a year (so $\mathscr{P}$ is sometimes called the "stroboscopic map", Crawford, 1991). Annual cycles of the original system correspond to fixed points of $\mathscr{P}$, biennial cycles to two-point cycles, and so on. Stability of cycles of the original system correspond to stability of the associated periodic points of $\mathscr{P}$. Attraction or repulsion of cycles of the original system is determined by the system's Floquet multipliers, which are equal to the eigenvalues of $D\mathscr{P}$, the Jacobian matrix of $\mathscr{P}$, at the associated periodic points

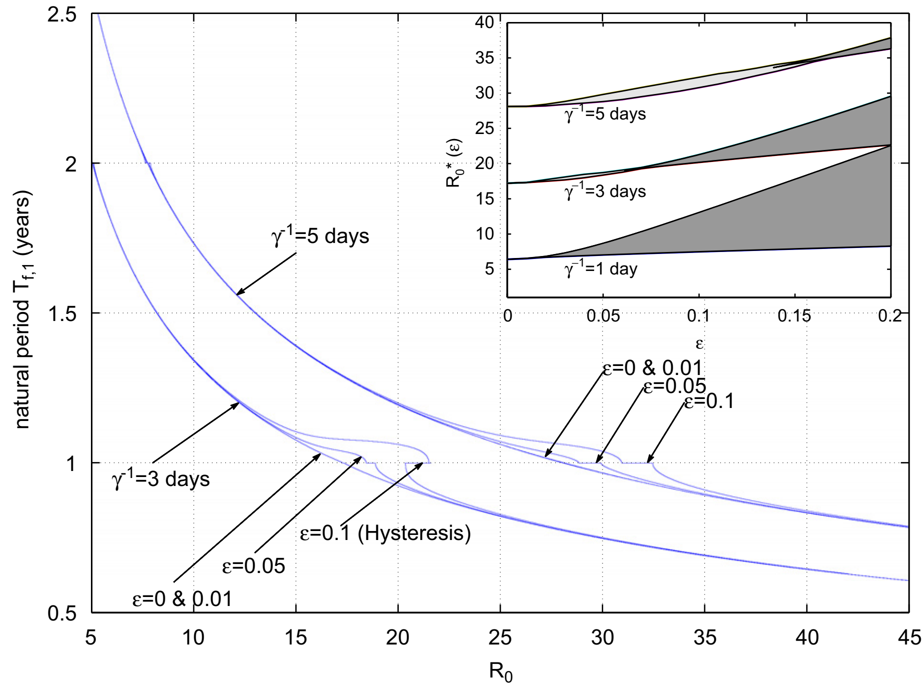

Fig. 6. Resonant effects associated with the annual cycle attractor of the SIR model (7) with birth seasonality. The main panel shows the natural period of damped oscillations ($2\pi/\omega$) versus the basic reproductive ratio ($\mathscr{R}_0$) for different amplitudes of birth seasonality (ε) and different mean infectious periods (four curves are shown for $\gamma^{-1} = 3$ days and four curves are shown for $\gamma^{-1} = 5$ days). The inset panel shows resonant reproductive ratios $\mathscr{R}_0^*$ (which yield period $2\pi/\omega = 1$ yr) as a function of ε. In the limit $\varepsilon \to 0$, there is a single resonant reproductive ratio (Eq. (25)), whereas for larger ε, there are resonant intervals of $\mathscr{R}_0$ associated with phase-locking and hysteresis (regions of the parameter space that yield hysteresis are shaded dark grey; phase-locked regions are shaded light grey). The method used to estimate the frequency ω when $\varepsilon > 0$ is discussed in Section 4.3.

(e.g., Guckenheimer and Holmes, 1983, p. 25; Kuznetsov, 1995, Theorem 1.6).

Consider a periodic point of the Poincaré map $\mathscr{P}$, i.e., a point (S_0, I_0) that lies on a periodic solution $(\bar{S}(t), \bar{I}(t))$ of the original system (7) (for convenience we assume $\bar{S}(0) = S_0$ and $\bar{I}(0) = I_0$). The entries of the Jacobian matrix $D\mathscr{P}(S_0, I_0)$ can be obtained numerically as follows. Similar to the variational equations (11) for the unforced SIR model about the equilibrium $(\hat{S}, \hat{I})$, we have variational equations associated with the seasonally forced SIR model (7) along the periodic solution $(\bar{S}(t), \bar{I}(t))$,

$$\begin{pmatrix} \dot{\Delta S} \\ \dot{\Delta I} \end{pmatrix} = \begin{pmatrix} -\nu(\mathscr{R}_0\mathscr{G}\bar{I}(t)+1) & -\nu\mathscr{R}_0\mathscr{G}\bar{S}(t) \\ \nu\mathscr{R}_0\mathscr{G}\bar{I}(t) & \nu\mathscr{G}(\mathscr{R}_0\bar{S}(t)-1) \end{pmatrix} \begin{pmatrix} \Delta S \\ \Delta I \end{pmatrix}. \tag{31}$$

(Note that in the limit $\varepsilon \to 0$, the periodic solution $(\bar{S}(t), \bar{I}(t))$ reduces to the equilibrium $(\hat{S}, \hat{I})$ and the variational equations (31) reduce to Eq. (11) for the unforced SIR model.) If we determine how an arbitrary deviation $(\Delta S, \Delta I)$ from (S_0, I_0) is mapped forward in time by 1 yr then we will have calculated the entries of the Jacobian matrix $D\mathscr{P}(S_0, I_0)$ (e.g., Kuznetsov, 1995, Theorem 1.6). This can be done most easily in two steps, first integrating (31) from $(\Delta S, \Delta I) = (1, 0)$ for 1 yr, and then from $(\Delta S, \Delta I) = (0, 1)$ for 1 yr (thus obtaining the first row and then the second row of $D\mathscr{P}(S_0, I_0)$).

Writing the Jacobian $J = D\mathscr{P}(S_0, I_0)$, its eigenvalues are

$$\Lambda_\pm = \begin{cases} \frac{1}{2}[\operatorname{tr} J \pm i\sqrt{4\det J - (\operatorname{tr} J)^2}] & \text{if } 4\det J \geqslant (\operatorname{tr} J)^2, \\ \frac{1}{2}[\operatorname{tr} J \pm \sqrt{(\operatorname{tr} J)^2 - 4\det J}] & \text{if } 4\det J < (\operatorname{tr} J)^2. \end{cases} \tag{32}$$

We calculated these eigenvalues by integrating the variational equations as described above, and verified that our computations were correct by calculating the Floquet multipliers independently using CONTENT 1.5 (Kuznetsov, 1995).

The frequency of damped (or growing) oscillations of trajectories that begin near the periodic point (S_0, I_0) is

$$\omega = \begin{cases} k\pi + \arctan\left(\sqrt{4\det J - (\operatorname{tr} J)^2}/\operatorname{tr} J\right) & \text{if } 4\det J \geqslant (\operatorname{tr} J)^2, \\ k\pi & \text{if } 4\det J < (\operatorname{tr} J)^2. \end{cases} \tag{33}$$

Here, the integer k provides the information that cannot be provided by the arctan function, which has range $(-\pi/2, \pi/2)$, i.e., k is the number of half rotations around the periodic point (S_0, I_0) that the orbit completes between the time points considered in the stroboscopic map (see Fig. 7). We are not concerned with the sense of this rotation, so we ignore the sign of ω (equivalently, we can

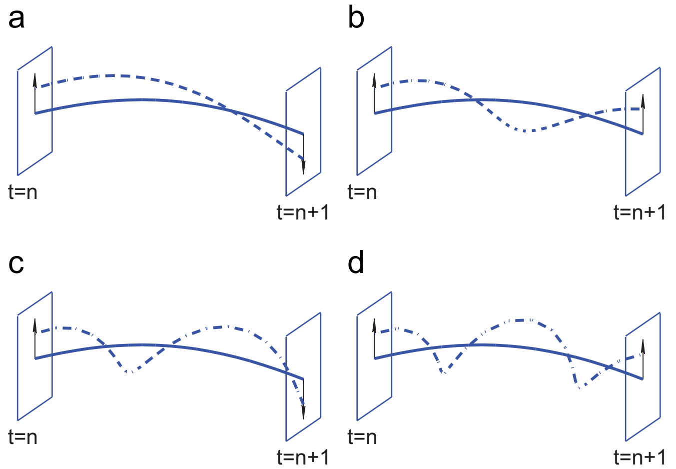

Fig. 7. Schematic illustrations of the types of dynamics that can occur between the stroboscopic snapshots associated with orbits that are close to fixed points of the Poincaré map $\mathscr{P}$ (i.e., in the neighbourhood of an annual cycle of the full system). Solid lines denote an annual cycle. Dash-dotted lines denote a neighbouring orbit. Arrows illustrate the initial and final variations (ΔS, ΔI). The integer k is the number of half rotations that the neighbouring orbit completes between snapshots of the stroboscopic map. (a) $\omega = \pi$ ($k = 1$), (b) $\omega = 2\pi$ ($k = 2$), (c) $\omega = 3\pi$ ($k = 3$), and (d) $\omega = 4\pi$ ($k = 4$).

take the absolute value of the arctan in Eq. (33) and assume $k \geqslant 0$).

In the first case in Eq. (33) (where the eigenvalues of J have a non-zero imaginary part) the period $T = 2\pi/\omega$ can take any (positive) real value. In the second case, however, the eigenvalues of J are purely real and ω can take only discrete values (even though the entries of J can be varied continuously).

To identify resonance, we explore ranges of the parameters ($\mathscr{R}_0$, γ, ε), computing ω as above for each parameter set, and noting parameter values that yield $\omega = 2\pi$ (i.e., $4 \det J = (\operatorname{tr} J)^2$ and $k = 2$). In practice, to construct Fig. 6, we fixed γ and ε and computed ω as we varied $\mathscr{R}_0$, to identify resonant reproductive ratios $\mathscr{R}_0^*$.

4.4. *SIR dynamics with large birth seasonality amplitude* ε

Because birth seasonality in Canada and the United States currently has amplitude $\varepsilon \lesssim 0.1$, we have focused our attention so far on small and modest levels of seasonal forcing ($\varepsilon \lesssim 0.1$). In order to develop a complete understanding of the possible role of birth seasonality, we need to explore larger ε and establish whether greater birth seasonality can induce dynamics that are more complex than the annual limit cycles investigated in previous sections. In this section, we use CONTENT 1.5 (Kuznetsov, 1995) to examine the qualitative dynamics of the SIR model with large seasonal forcing of the birth rate.

Fig. 8 summarizes the dynamics of the model for fixed (large) values of the seasonal amplitude ε. Fig. 8a shows a bifurcation diagram with control parameter $\mathscr{R}_0$, with $\varepsilon = 0.5$ and mean infectious period $\gamma^{-1} = 5$ days. The curves show the proportion of individuals infectious on 1 January, so single points indicate an annual cycle, two points indicate a biennial cycle, and so on. Stable and unstable branches are indicated by solid and dotted curves, respectively. Several bifurcations are evident and there is a range of $\mathscr{R}_0$ over which there are coexisting stable annual and biennial cycles. The basin of attraction of the biennial attractor at $\mathscr{R}_0 = 12$ is shown in Fig. 8b.

Figs. 8c and d show two-parameter bifurcation diagrams for $\varepsilon = 0.3$ and 0.6, respectively. In each of these diagrams, three distinct parameter regions are identified: (I) a unique (annual) attractor exists, (II) a unique (biennial) attractor exists, and (III) an annual and biennial attractor coexist.

Fig. 9 examines how the dynamics of the birth forced SIR model vary over the full range of forcing amplitudes, $0 \leqslant \varepsilon \leqslant 1$, and a wide range of reproductive ratios $\mathscr{R}_0$, with the mean infectious period fixed at $\gamma^{-1} = 5$ days. Fig. 9a shows a two-parameter bifurcation diagram, with regions labelled using the same convention as just described for Figs. 8c and d. Figs. 9b, c, and d show representative one-parameter bifurcation diagrams (control parameter ε), displaying the different characters of period-doubling bifurcations that occur as we cut horizontally through Fig. 9a at $\mathscr{R}_0 = 7.5$, 8, and 10, respectively. Fig. 9e shows that horizontal cuts through the type of two-parameter bifurcation diagram shown in Fig. 9a will produce either period-doubling or hysteresis (but not both) depending on the fixed value of γ^{-1}.

Finally, Fig. 10 shows how the dynamics of the model vary as a function of seasonal amplitude ε and mean infectious period γ^{-1}, for fixed $\mathscr{R}_0$. The main panels show two-parameter bifurcation diagrams for $\mathscr{R}_0 = 10$, 20, and 30, respectively. In panels a and b, entering the triangular region bounded by the curve marked PDU (for "period-doubling upper") corresponds to changing from a stable annual to stable biennial cycle. This PDU curve is shown for several values of $\mathscr{R}_0$ on the small panel inset to panel a (this period-doubling bifurcation does not occur for $\mathscr{R}_0 \gtrsim 28$).

A second period-doubling bifurcation curve marked PDL (for "period-doubling lower") is shown in each of the three main panels of Fig. 10. This is also a bifurcation from a stable annual to stable biennial cycle. In addition, there are two curves corresponding to fold bifurcations, where an annual cycle changes stability (these curves are marked LPU and LPL for "limit point upper" and "limit point lower"). In Fig. 10c, the dotted horizontal line at the very short infectious period of 0.8 day corresponds to the one-parameter bifurcation diagram inset in the upper right of this panel. In this small inset panel, three bifurcations are marked (two folds marked LP1 and LP2 and a period-doubling bifurcation marked PD) and the corresponding points along the dotted line in the main panel are also marked. Note that in this (unrealistic) extreme with $\mathscr{R}_0 = 30$ and $\gamma^{-1} = 0.8$ day, there is a narrow range of seasonal amplitude, $0.729 < \varepsilon < 0.774$, over which there is coexistence of a stable annual cycle, a stable biennial cycle, and two

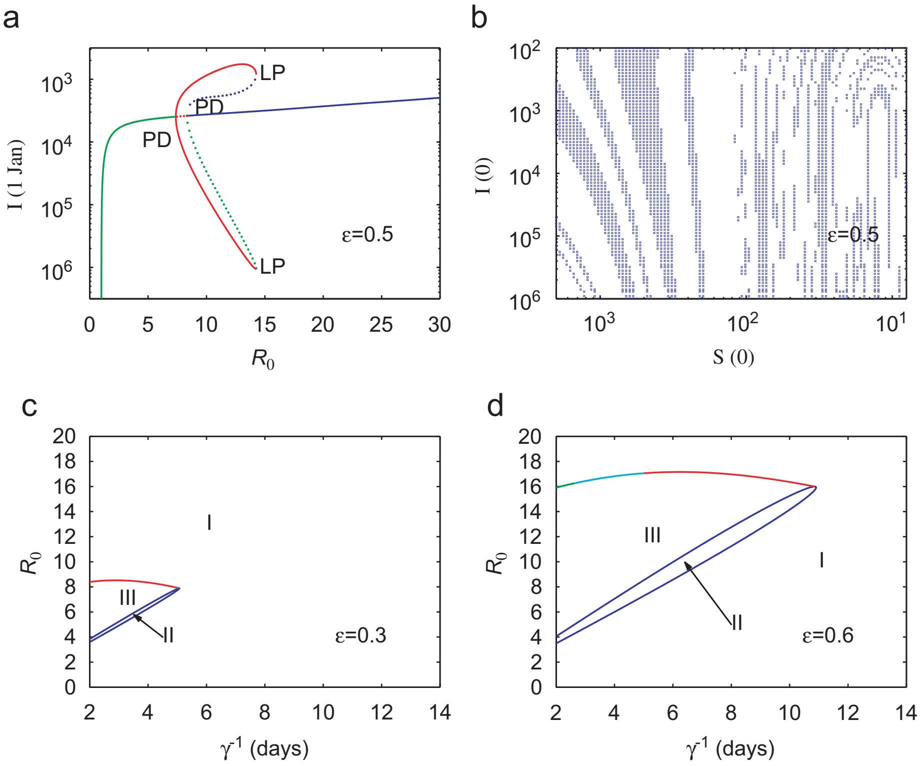

Fig. 8. Bifurcations of the SIR model (7) with large birth seasonality ε. Panel (a) shows period-doubling in a one-parameter bifurcation diagram with control parameter $\mathscr{R}_0$ ($\varepsilon = 0.5$, $\gamma^{-1} = 5$ days, $\nu = 0.02\,\mathrm{yr}^{-1}$); to obtain this diagram, the system is strobed annually on 1 January. Two period-doubling points (PD) and two limit points (LP) where stable (solid curves) and unstable (dotted curves) period 2 branches merge are shown. Panel (b) shows the basin of attraction of the period 2 attractor associated with $\mathscr{R}_0 = 12$ in panel (a). Panels (c) and (d) show two-parameter (γ^{-1} versus $\mathscr{R}_0$) bifurcation diagrams, for $\varepsilon = 0.3$ and 0.6. These diagrams were created with CONTENT 1.5 by continuation of the period-doubling and limit points shown in panel (a). In panels (c) and (d), a stable period 1 attractor exists in regions I and III but not in region II, while a stable period 2 attractor exists in regions II and III but not in region I.

unstable annual cycles; as ε is increased further, there is a period-doubling cascade to chaos (not shown).

4.5. *Bifurcations and phase-locked transients*

The central panel b of Fig. 10 contains some dash-dotted curves that help to explain the circumstances under which the observed bifurcations can occur.

Throughout the triangular parameter region at the top of Fig. 10b (the region bounded by dash-dotted curves and marked "$\omega = \pi$") the transient dynamics are locked onto a period of exactly $T = 2\pi/\omega = 2\,\mathrm{yr}$. It is easy to see that period-doubling bifurcations can occur only within such a phase-locked region, as follows.

Period-doubling bifurcations occur when a single (multiplicity 1) eigenvalue of J passes out of the unit circle through -1, destabilizing a cyclical solution of the SIR model (7) (a periodic point of $\mathscr{P}$). When this occurs, the other eigenvalue of J must have magnitude less than 1 and must lie on the real line (because complex eigenvalues come in conjugate pairs). Since the eigenvalues are continuous functions of the matrix entries (which are continuous functions of the model parameters) the eigenvalues must be real just before the bifurcation. Thus, period-doubling bifurcations can occur only in the interior of regions of parameter space where the eigenvalues of J are real. But in such regions, the angular frequency ω can take only a discrete set of values (Eq, (33)), hence period-doublings can occur only in parameter regions where transients are phase-locked.

The same argument applies to fold or "saddle-node" bifurcations (marked LP for "limit point" in our diagrams) where there is a change in the stability of a periodic point of $\mathscr{P}$ (without a change in period). Folds occur where a single eigenvalue of J passes out of the unit circle through 1, so—like period-doubling bifurcations—they can occur only in the interior of regions of parameter space where the eigenvalues of J are real, and hence where transients are phase-locked.

Any given periodic solution is characterized not only by the integer period that is observable from the stroboscopic map $\mathscr{P}$, but by the number of half rotations k that it completes between successive strobes (Eq. (33)). For a given set of parameters, multiple periodic solutions can occur, with different basins of attraction. Thus, a given parameter set can correspond to several periodic solutions with different k, associated with different initial conditions. In general, associated with each positive integer k there is a region of parameter space within which the eigenvalues of J are real and period-doubling (k odd) or fold (k even)

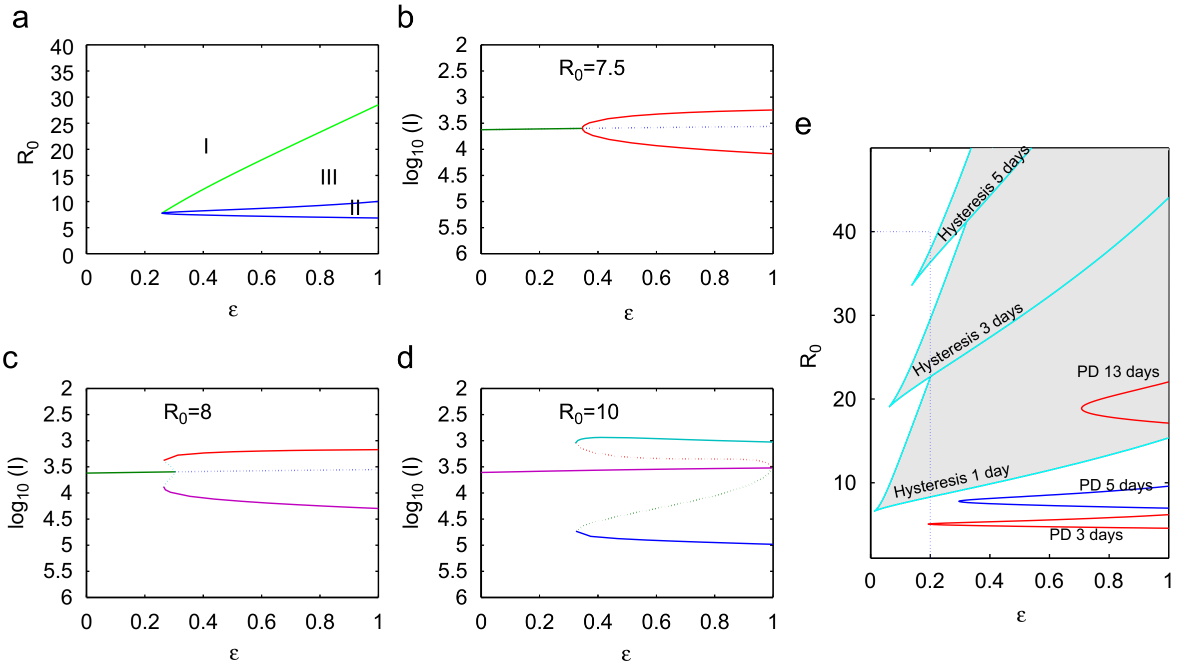

Fig. 9. Bifurcations of the SIR model (7) with birth seasonality, in the ε versus $\mathscr{R}_0$ parameter plane. Panel (a) is coded similarly to panels (c) and (d) of Fig. 8; stable annual cycles exist in regions I and III but not in region II, while stable biennial cycles exist in regions II and III but not in region I (the infectious period is fixed at $\gamma^{-1} = 5$ days in these diagrams). Panels (b), (c), and (d) show one-parameter bifurcation diagrams that correspond to horizontal cuts through panel (a) at $\mathscr{R}_0 = 7.5$, 8, and 10; as usual, solid lines denote stable solutions while dotted lines denote unstable solutions. Panel (e) shows the hysteresis region (shaded grey) and period-doubling points in the $\mathscr{R}_0$ versus ε plane, for several values of γ^{-1}. The rectangular region marked with dotted lines ($0 \leqslant \varepsilon \leqslant 0.2$ and $1 \leqslant \mathscr{R}_0 \leqslant 40$) corresponds to the inset panel of Fig. 6.

bifurcations can occur. These parameter regions associated with different k can overlap, as the numerical example in Fig. 10b shows (the phase-locked regions for $\omega = \pi, 2\pi, 3\pi$, and 4π are shown). In the limit of no seasonal forcing ($\varepsilon \to 0$), each such region connects to the mean infectious period (γ^{-1}) that yields an angular frequency of $k\pi$ in the unforced model.

The arguments in this section have nothing to do with birth rate forcing *per se* or the SIR model specifically. They apply generally regardless of the nature of the seasonal forcing and the details of the model. Consequently, we can make a more general inference.

Theorem 1. *In a periodically forced continuous-time smooth dynamical system, period-doubling and fold bifurcations occur only in regions of parameter space where transients are phase-locked onto periods that exactly divide the forcing period.*

5. The SEIR model with seasonal oscillation in birth rate

When we use the SIR model (7), we are implicitly making the approximation that the latent period (the time between initial infection and becoming infectious) is zero. For childhood diseases, the latent period is often comparable to the infectious period (Anderson and May, 1991), so assuming a zero latent period might be a poor approximation.

Non-zero latency is usually introduced by adding an "exposed" (E) compartment in which individuals are infected but not yet infectious. If the rate at which exposed individuals become infectious is σ (so the mean latent period is σ^{-1}) then the expanded model can be written as

$$\dot{S} = v - (\beta I + v)S, \tag{34a}$$

$$\dot{E} = \beta IS - (\sigma + v)E, \tag{34b}$$

$$\dot{I} = \sigma E - (\gamma + v)I, \tag{34c}$$

$$\dot{R} = \gamma I - vR, \tag{34d}$$

where we assume from the outset that state variables refer to proportions, so $S + E + I + R = 1$ (consequently, one of the differential equations is redundant and usually Eq. (34d) is ignored).

The basic reproductive ratio for the SEIR model is

$$\mathscr{R}_0 = \frac{\beta\sigma}{(\gamma + v)(\sigma + v)}. \tag{35}$$

For any $\mathscr{R}_0$ there is a globally asymptotically stable equilibrium (Li and Muldowney, 1995; Korobeinikov and Maini, 2004). If $\mathscr{R}_0 \leqslant 1$ then the DFE is stable, whereas if $\mathscr{R}_0 > 1$ then there is a stable endemic equilibrium $(\hat{S}, \hat{E}, \hat{I})$:

$$\hat{S} = \frac{1}{\mathscr{R}_0}, \tag{36a}$$

$$\hat{E} = \frac{v}{\sigma + v}(1 - \hat{S}) = \frac{v}{\sigma + v}\left(1 - \frac{1}{\mathscr{R}_0}\right), \tag{36b}$$

$$\hat{I} = \frac{\sigma}{\gamma + v}\hat{E} = \frac{\sigma v}{(\gamma + v)(\sigma + v)}\left(1 - \frac{1}{\mathscr{R}_0}\right). \tag{36c}$$

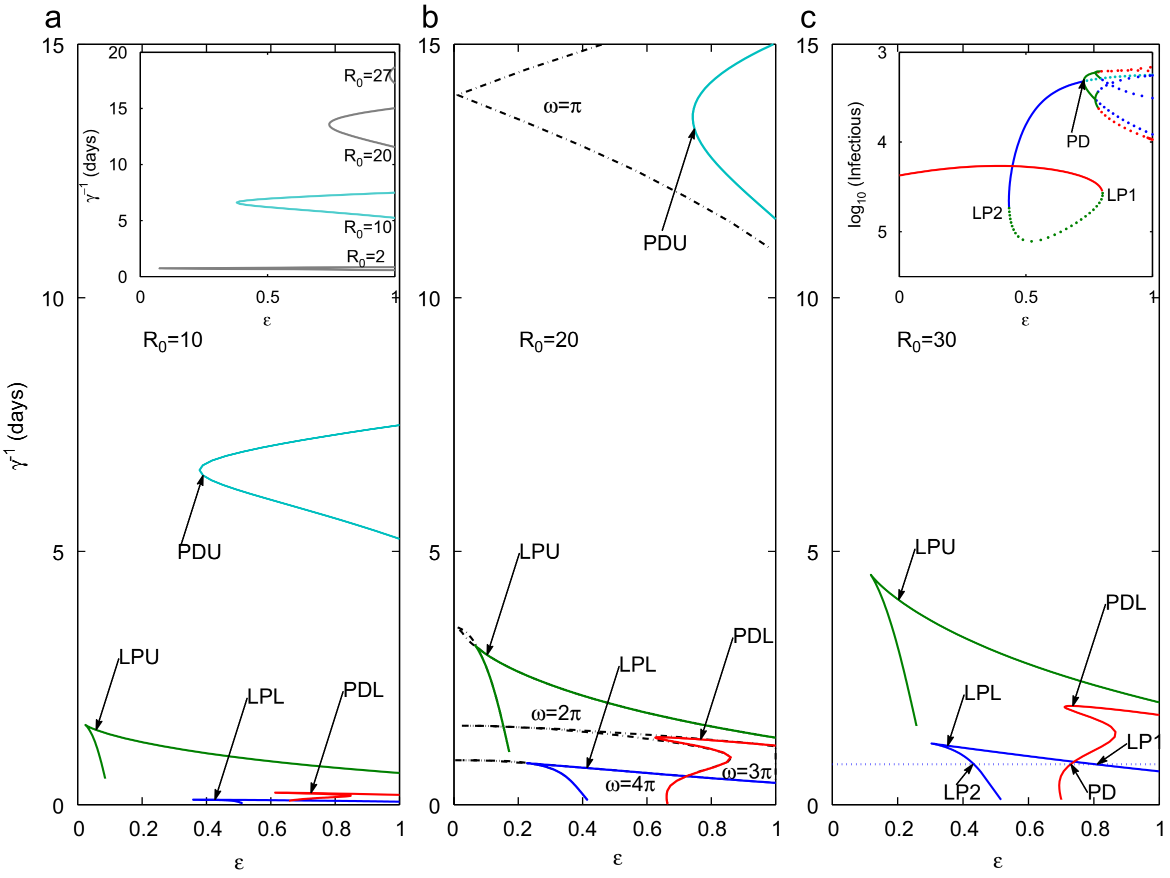

Fig. 10. Bifurcations of the SIR model (7) with birth seasonality, in the ε versus γ^{-1} plane. The three main panels show two-parameter bifurcation diagrams with $\mathscr{R}_0$ fixed at 10, 20, and 30, respectively. Period-doubling and fold bifurcations (of annual cycles) are marked in each case (with an L for "lower" or U for "upper" appended to the standard annotation PD or LP). The inset to panel (a) shows how the period-doubling bifurcation curves vary as a function of $\mathscr{R}_0$ (this bifurcation does not occur for $\mathscr{R}_0 \gtrsim 28$). In panel (b), in addition to the bifurcation curves, regions in which transients about the annual cycle are phase-locked are identified by dash-dotted curves; as discussed in Section 4.5, period-doubling and fold bifurcations can occur only within such phase-locked regions. In panel (c), with $\mathscr{R}_0 = 30$ ($\gtrsim 28$), there is no upper period-doubling bifurcation (PDU). The inset to panel (c) shows the one-parameter bifurcation diagram corresponding to the horizontal cut through the main panel that is marked with a dotted line (at $\gamma^{-1} = 0.8$ day). Two folds occur, at $\varepsilon = 0.803$ (LP1) and $\varepsilon = 0.433$ (LP2), and a period-doubling (from annual to biennial cycle) occurs at $\varepsilon = 0.729$ (PD); further increase of ε leads to a period-doubling cascade to chaos.

The eigenvalues of the Jacobian matrix associated with the linearization of Eqs. (34) about the endemic equilibrium $(\hat{S}, \hat{E}, \hat{I})$ can be obtained exactly but are unwieldy. Useful, simple approximate expressions for the eigenvalues can be obtained by treating the birth rate v as a small parameter (which is always justified for childhood diseases, for which $v \ll \gamma \sim \sigma$). Standard methods yield (Schwartz and Smith, 1983; Bauch and Earn, 2003)

$$\lambda_1 = -(\sigma + \gamma) + O(v), \tag{37a}$$

$$\lambda_+ = i\tilde{\omega}\sqrt{v} - \tilde{r}v + O(v^{3/2}), \tag{37b}$$

$$\lambda_- = -i\tilde{\omega}\sqrt{v} - \tilde{r}v + O(v^{3/2}), \tag{37c}$$

where

$$\tilde{r} = \frac{1}{2}\left(\mathscr{R}_0 - \frac{\sigma\gamma(\mathscr{R}_0 - 1)}{(\sigma + \gamma)^2}\right), \quad \tilde{\omega} = \sqrt{\frac{\mathscr{R}_0 - 1}{1/\sigma + 1/\gamma}}. \tag{38}$$

In the limit of zero latent period ($\sigma \to \infty$), the decay rate $r = \tilde{r}v$ and the angular frequency $\omega = \tilde{\omega}\sqrt{v}$ agree with Eqs. (12b) and (12c) for the corresponding quantities associated with the SIR model (7). Note that we also obtain the equivalent of Eq. (14) if we replace $\mathscr{G}$ (defined in Eq. (9)) with

$$\mathscr{G}' = \left(\frac{v}{\sigma + v} + \frac{v}{\gamma + v}\right)^{-1}. \tag{39}$$

If births balance deaths ($\mu = v$) then $\mathscr{G}$ is the mean lifetime expressed in units of the mean time an individual is infectious, whereas $\mathscr{G}'$ is the mean lifetime expressed in units of the mean time an individual is infected (latent or infectious).

In addition to the two complex conjugate eigenvalues $\lambda_\pm$, the inclusion of an exposed class yields the (real) eigenvalue λ_1. Since the leading term of λ_1 does not contain a power of v, the magnitude of λ_1 is much larger than the other eigenvalues. Consequently, in the neighbourhood of the endemic equilibrium, there is rapid collapse onto a centre manifold where the dynamics are governed by $\lambda_\pm$, as for the SIR model. The expression for the angular frequency ω for the SEIR model (38) differs from the corresponding expression for the SIR model (12c) only in that the sum of the latent and infectious periods $(1/\sigma + 1/\gamma)$ replaces the infectious period alone $(1/\gamma)$ (this is noted in Anderson and May, 1991, p. 668). The non-zero latent period also has the effect of reducing the decay rate r, so transients in the neighbourhood of the equilibrium will decay more slowly. For childhood diseases, the latent and infectious periods are of the same order of magnitude, so $\sigma\gamma/(\sigma+\gamma)^2 \sim \gamma^2/(2\gamma)^2 = \frac{1}{4}$; hence the reduction in r in Eq. (38) relative to Eq. (12b) is of order 25%. Thus, near the endemic equilibrium, the dynamics of the SEIR model will be nearly the same as the SIR model *provided* that we use an infectious period in the SIR that corresponds to the sum of the true latent and infectious periods of the disease. This remark motivates using a mean infectious period of 13 days when using the SIR equations (7) to model measles (for which $\sigma^{-1} \simeq 5$ days and $\gamma^{-1} \simeq 8$ days).

Taking advantage of the fact that ν is small relative to γ and σ (hence using expression (38) for $\tilde{\omega}$) we can easily approximate the resonant reproductive ratio $\mathcal{R}_0^*$ by setting $\tilde{\omega}\sqrt{\nu} = 2\pi/t_{\mathrm{f}}$ which yields

$$\mathcal{R}_0^* \simeq 1 + \frac{4\pi^2}{t_{\mathrm{f}}^2 \nu}\left(\frac{1}{\sigma} + \frac{1}{\gamma}\right) \simeq 1 + \frac{4\pi^2}{\nu^2 t_{\mathrm{f}}^2 \mathcal{G}'}. \tag{40}$$

Eq. (40) agrees with Eq. (25) in the limit $\sigma \to \infty$ (bearing in mind that we obtained expression (40) by neglecting ν relative to γ and σ). This comparison of the expressions for $\mathcal{R}_0^*$ emphasizes that if we want to study resonance of childhood diseases using the SIR model, then we must take the mean infectious period in the SIR model to be the sum of the true mean latent and infectious periods. In general, note that larger latent or infectious periods correspond to larger resonant reproductive ratios.

Fig. 11 shows resonance in the SEIR model with birth seasonality $\varepsilon = 0.04$. Fig. 11a (where $\gamma^{-1} = 5$ days and $\sigma^{-1} = 8$ days) is the SEIR equivalent of Fig. 5a (where $\gamma^{-1} = 13$ days) for the SIR model. The difference between Figs. 11a and 5a is small: at the resonant reproductive ratio $\mathcal{R}_0^*$, the amplitude α_S in the SEIR case is larger than one, whereas $\alpha_S(\mathcal{R}_0^*) \simeq 1$ in the SIR case (Fig. 5a). We note that in the SEIR case, if $\mathcal{R}_0 = \mathcal{R}_0^*/2$ then the amplitude α_I is still close to one, as for the SIR model.

Fig. 11b shows (for the SEIR model) how the shape quotient Q_ε depends on the mean infectious period γ^{-1} and should be compared with Figs. 4b and c for the SIR model. The different curves in Fig. 11b correspond to different mean latent periods ($\sigma^{-1} = 0$, 1, 5, and 8 days), with a zero latent period corresponding to the SIR model. Fig. 11c shows the same points plotted as a function of $\sigma^{-1} + \gamma^{-1}$ rather than γ^{-1}, making clear (again) that there is really no

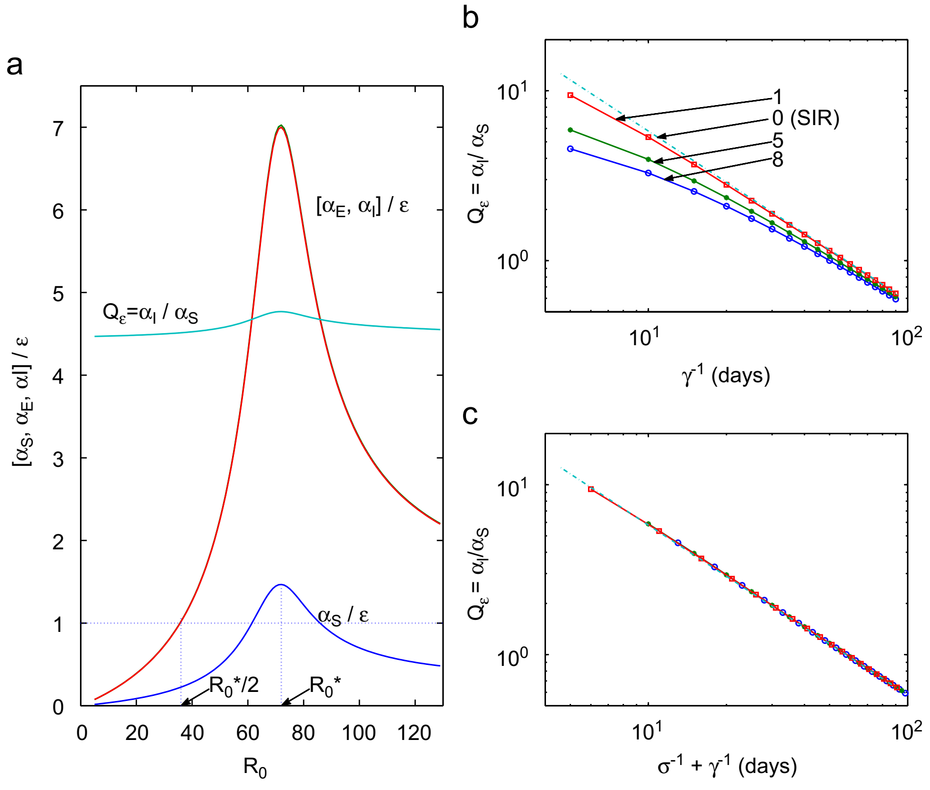

Fig. 11. Resonance in the SEIR model (34) with seasonal variation in birth rate ($\varepsilon = 0.04$). Panel (a) (where $\gamma^{-1} = 5$ days and $\sigma^{-1} = 8$ days) should be compared with Fig. 5a for the SIR model (7), while panels (b) and (c) should be compared with Figs. 4b and c. In panel (b), the latent period (σ^{-1}) is marked for each curve. Panel (c), which shows the same information as panel (b), makes clear that no difference is evident between the results for the SIR and SEIR models, provided we associate $\sigma^{-1} + \gamma^{-1}$ in the SEIR model with γ^{-1} in the SIR model.

discernable difference between the behaviour of the SIR and SEIR models if we associate the mean *infectious* period in the SIR model with the mean *infected* period in the SEIR model.

6. Discussion

We have investigated the effects of seasonal oscillations in birth rate on infectious disease transmission dynamics. In Section 2 we found that in North America the amplitude of oscillations is on the order of 10% of the mean birth rate ($\varepsilon \sim 0.1$). In Section 4, analysis of the SIR epidemic model in the presence of birth seasonality revealed a number of potentially significant dynamical effects, depending on the characteristics of the disease in question. In Section 5, we found that predictions based on the (more realistic) SEIR model (34) will be essentially the same as those based on the SIR model (7) if the parameter γ^{-1} in the SIR model is interpreted as the sum of the mean latent and infectious periods.

Estimates of the mean latent period σ^{-1}, mean infectious period γ^{-1}, and basic reproductive ratio $\mathscr{R}_0$ are given for a variety of childhood infectious diseases in Table 1. In addition, the table shows the resonant reproductive ratio $\mathscr{R}_0^*$ (Eq. (40)) associated with the estimated latent and infectious periods. In all cases, the observed reproductive ratio is far from $\mathscr{R}_0^*$, so in situations where the amplitude of seasonality is small (i.e., the limit in which the expression for $\mathscr{R}_0^*$ was derived) we do not expect significant amplification of oscillations in incidence.

For places where the amplitude of birth seasonality is similar to what is currently observed in North America ($\varepsilon \sim 0.1$), Fig. 3 shows that all of the diseases listed in Table 1 are still far from the range of $\mathscr{R}_0$ that would yield resonance and hysteresis (resulting from fold bifurcations). From another perspective, the fact that substantial seasonal amplitudes tend to bend the resonance curve to the right (Fig. 5b) means that the resonant reproductive ratio calculated from the unforced model will always tend to underestimate $\mathscr{R}_0^*$.

Table 1
Parameter estimates for several childhood infectious diseases, taken from Table 3.1 of Anderson and May (1991)

Disease	σ^{-1} (days)	γ^{-1} (days)	$\mathscr{R}_0$	$\mathscr{R}_0^*$
Measles	8	5	16–18	72
Whooping cough	8	14	16–18	123
Chickenpox	14	7	10–12	117
Rubella	7–14	11–14	6–7	100–160
Mumps	13	6	11–14	106
Polio	1–3	14–20	6–7	83–129
Scarlet fever	1–2	14–21	7–8	83–130

Mean latent period (σ^{-1}), mean infectious period (γ^{-1}), and basic reproductive ratio ($\mathscr{R}_0$). $\mathscr{R}_0^*$ is the resonant reproductive ratio given by Eq. (40) based on the mean latent and infectious periods estimated for each disease.

When calculating the resonant reproductive ratio $\mathscr{R}_0^*$ numerically (e.g., Figs. 5a and b), we discovered a scaling relationship that is shown in Fig. 12 (based on the SEIR model). This figure shows how the amplitudes of seasonal oscillations in susceptibles and infectives (relative to the amplitude of birth seasonality ε) change as a function of the sum of the mean latent and infectious periods of the disease ($\sigma^{-1} + \gamma^{-1}$). The plotted points (which correspond to mean latent and infectious periods of a variety of childhood infections) represent the induced oscillations in susceptibles (α_S/ε, panel a) and infectives (α_I/ε, panel b) when the reproductive ratio is set to exactly half the resonant value ($\mathscr{R}_0 = \mathscr{R}_0^*/2$, which is still larger than any observed $\mathscr{R}_0$ for these diseases). For susceptibles, a linear scaling is evident, whereas for infectives the amplitude of oscillations in I are the same as those in births ($\alpha_I/\varepsilon = 1$) regardless of the latent and infectious periods. Figs. 12c and d show that the value $\mathscr{R}_0 = \mathscr{R}_0^*/2$ used for Figs. 12a and b is special in that $\alpha_I/\varepsilon = 1$ holds almost exactly. For other values of $\mathscr{R}_0$, the relationship between α_I/ε and $\sigma^{-1} + \gamma^{-1}$ is linear (provided $\mathscr{R}_0 \lesssim 0.7\,\mathscr{R}_0^*$), but the slope and intercept of the best fit line varies (the slope is always small, so α_I/ε never varies substantially as a function of $\sigma^{-1} + \gamma^{-1}$).

Further analysis revealed that birth seasonality can induce a variety of fold and period-doubling bifurcations, but primarily at very short infectious periods or very large amplitudes of birth seasonality (Fig. 10). Nevertheless, analysis of transient dynamics revealed that solutions can be phase-locked onto cycles with periods that differ from the attractors to which they converge. If these transients are sustained by noise (Bartlett, 1960; Bauch and Earn, 2003) then significant dynamical effects of birth rate seasonality on incidence patterns might be observable for some diseases, even for small amplitude oscillations in birth rate. In particular, for the case of measles (taking $\gamma^{-1} = 13$ days in the SIR model), Fig. 10b suggests that small amplitude birth seasonality could induce stochastically sustained cycles that are approximately biennial.

The effects of birth seasonality on infectious disease dynamics have been investigated previously for fatal diseases of wildlife with relatively short lifespans, such as haemorrhagic fever in rabbits (Ireland et al., 2004). Another study considered the effects of strictly seasonal (pulsed) births on animal diseases, which is relevant to diseases such as tuberculosis in the possum (Roberts and Kao, 1998). In these contexts, the reproductive rate of the host population is density dependent and the average reproductive rate of hosts is influenced by seasonal forcing of the birth rate. Effects on host population dynamics resulting from a combination of seasonality of host reproduction and macroparasitic infections (e.g., nematodes) have also been explored (White et al., 1996). In the context of human diseases, which has been our focus, host reproduction is not density dependent and the average host reproductive rate is not affected by birth rate

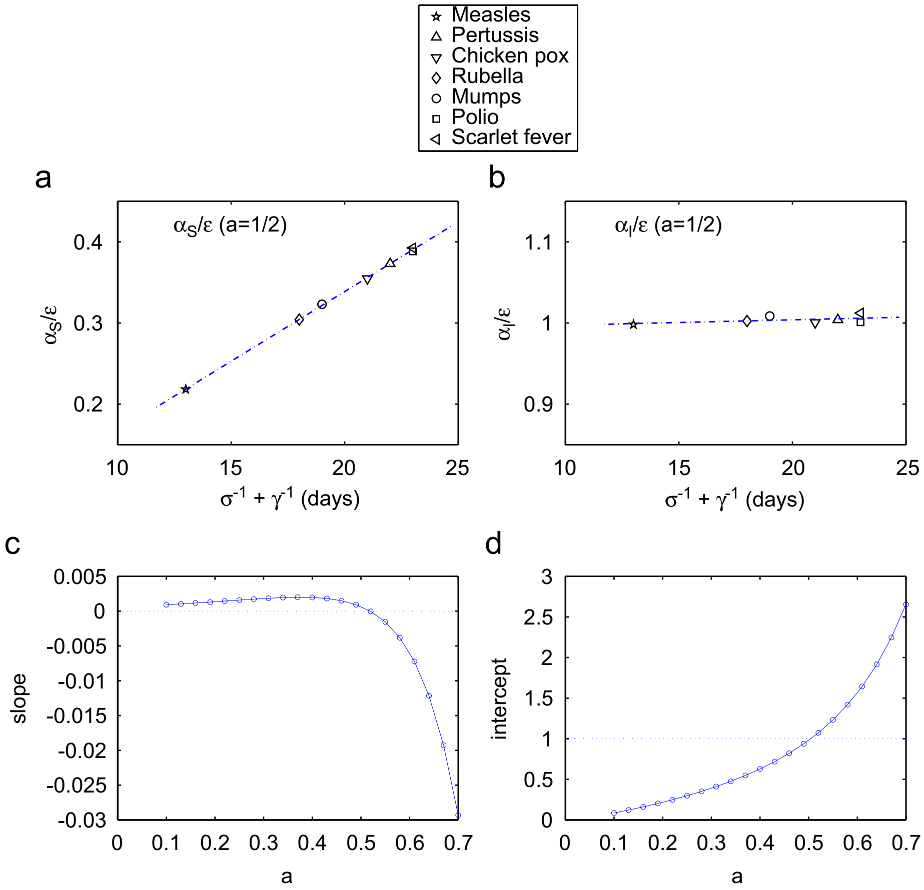

Fig. 12. Oscillation amplitudes as a function of mean time infected ($(\sigma^{-1}+\gamma^{-1})$) in the SEIR model (34) with realistic birth seasonality ($\varepsilon = 0.06$). Panels (a) and (b) show α_S/ε and α_I/ε, respectively. The infected periods of several childhood infectious diseases are identified. The basic reproductive ratio is set to $\mathcal{R}_0^*/2$ in all cases (see Eq. (40)). Panels (c) and (d) show how the slope and intercept of the relationship between $\sigma^{-1}+\gamma^{-1}$ and α_I/ε vary as a function of $a = \mathcal{R}_0/\mathcal{R}_0^*$. Near $a = \frac{1}{2}$ the slope is almost zero and the intercept is almost one, indicating that if $\mathcal{R}_0 = \mathcal{R}_0^*/2$ then the amplitude of oscillation in disease incidence is equal to the amplitude of oscillation in birth seasonality, for any latent and infectious periods. The horizontal axis range ends at $a = 0.7$ because for $a \gtrsim 0.7$ the relationships between oscillation amplitudes and time infected are no longer approximately linear. We have verified that similar results are obtained for other seasonal amplitudes $\varepsilon \leqslant 0.1$. For realistic $\mathcal{R}_0$ and $\varepsilon > 1$, phase-locking causes $\mathcal{R}_0^*$ to become a range rather than a single value (see Figs. 3 and 5), so a is not well defined and the picture is more complicated.

seasonality (because there is a long delay between birth and reproduction) nor by the type of infection we have considered (microparasites that cause relatively short respiratory infections).

Previous studies of the effects of seasonal forcing on childhood infectious disease dynamics have focused on seasonal variation in contact rates, which is believed to arise from aggregation of children during school terms (London and Yorke, 1973; Fine and Clarkson, 1982). Contact rate seasonality is traditionally modelled by making the transmission rate (β) vary seasonally in the SIR (7) or SEIR (34) models (London and Yorke, 1973; Schenzle, 1984; Olsen and Schaffer, 1990; Earn et al., 2000; Bauch and Earn, 2003). In this paper, we have examined the effects of seasonal forcing of the birth rate (v). A given amplitude of forcing applied to β tends to generate more exotic dynamics than applying the same level of forcing to v, probably because β occurs in a nonlinear term (βSI).

A natural extension of our work in this paper would be to consider the effects of forcing both β and v. Exploratory work that we have conducted suggests that forcing both parameters is most likely to generate important effects (such as hysteresis or coexistence of annual and biennial cycles) if there is a substantial phase difference between the two forcing functions. The true phase difference between birth rate seasonality and contact rate seasonality is different in different parts of the world, so the combined effects of these two seasonal influences may depend strongly on the region of interest. It might, therefore, be important to generalize methods that can reconstruct exogenous forcing functions from observed incidence data (Fine and Clarkson, 1982; Finkenstädt and Grenfell, 2000) so that both birth seasonality and contact seasonality can be estimated. Our exploratory work indicates that even with large phase differences between the two seasonal forcing functions, inclusion of birth seasonality will not have substantial effects on asymptotic dynamics for parameter ranges that correspond to known infectious diseases (consistent with our conclusions from the work presented in this paper).

A key conclusion of our analysis in this paper is that while strict resonance induced by seasonally varying birth rates is unlikely for diseases with realistic transmissibility, phase-locked transient dynamics can be induced by birth seasonality even for very weakly transmissible diseases. An important question for further work will be whether interaction between the two types of seasonal forcing (birth rate and transmission rate) substantially affects phase-locking regions, leading to greater or lesser likelihood of phase-locked transient patterns being sustained by demographic stochasticity.

Acknowledgment

We thank Chris Bauch, Paul Higgs, Nicholas Kevlahan, Junling Ma, James Watmough, Gail Wolkowicz, and two anonymous referees for helpful comments.

Appendix

If we expand the basic SIR model to include disease-induced mortality at rate m, our basic system of equations becomes

$$\dot{S} = \nu N - \beta SI/N - \mu S, \tag{41a}$$

$$\dot{I} = \beta SI/N - \gamma I - \mu I - mI, \tag{41b}$$

$$\dot{R} = \gamma I - \mu R, \tag{41c}$$

$$\dot{N} = (\nu - \mu)N - mI. \tag{41d}$$

If $m = 0$ then we have Eqs. (6). Note that the total host population size, $N = S + I + R$, is not constant unless $\nu = \mu$ and $m = 0$.

The rates of change of the proportions of the population in each compartment (S/N, I/N, R/N) are obtained by noting that

$$\frac{d}{dt}\left(\frac{X}{N}\right) = \frac{\dot{X}}{N} - \frac{X}{N^2}\dot{N}, \tag{42}$$

where X is S, I, or R. Putting this together with Eqs. (41) yields

$$\frac{d}{dt}\left(\frac{S}{N}\right) = \frac{1}{N}(\nu N - \beta SI/N - \nu S) + \frac{S}{N^2}mI, \tag{43a}$$

$$\frac{d}{dt}\left(\frac{I}{N}\right) = \frac{1}{N}(\beta SI/N - \gamma I - \nu I - mI) + \frac{I}{N^2}mI, \tag{43b}$$

$$\frac{d}{dt}\left(\frac{R}{N}\right) = \frac{1}{N}(\gamma I - \nu R) + \frac{R}{N^2}mI, \tag{43c}$$

$$\dot{N} = (\nu - \mu)N - mI. \tag{43d}$$

Rescaling variables, i.e., replacing X/N with X everywhere for $X = S$, I, or R, we obtain

$$\dot{S} = \nu - \beta SI - \nu S + mSI, \tag{44a}$$

$$\dot{I} = \beta SI - \gamma I - \nu I - m(1 - I)I, \tag{44b}$$

$$\dot{R} = \gamma I - \nu R + mRI, \tag{44c}$$

$$\dot{N} = (\nu - \mu - mI)N. \tag{44d}$$

If $m = 0$, Eqs. (44) are the same as Eqs. (7). If $m > 0$ then we note that the first two equations (which completely specify the dynamics) can be written as

$$\dot{S} = \nu - [\beta - m]SI - \nu S, \tag{45a}$$

$$\dot{I} = \beta SI - [\gamma + m(1 - I)]I - \nu I. \tag{45b}$$

Now, if P is the probability that an infected individual dies from the disease, then m must be of order γP (assuming the time to disease-induced death or recovery is similar). For the diseases of concern in this paper, $P \ll 1$, so we must have $\beta \gg m$ and $\gamma \gg m > m(1 - I)$. Consequently, the factors in square brackets in Eqs. (45) must be negligibly different from β and γ, respectively, and the full equations must be negligibly different from Eqs. (7). It is therefore unlikely that disease-induced mortality could have an observable influence on the dynamics explored in this paper.

References

Anderson, R.M., May, R.M., 1991. Infectious Diseases of Humans: Dynamics and Control. Oxford University Press, Oxford.

Bailey, N.T.J., 1975. The Mathematical Theory of Infectious Diseases and its Applications, second ed. Hafner Press, New York.

Bartlett, M.S., 1960. Stochastic Population Models in Ecology and Epidemiology. Methuen's Monographs on Applied Probability and Statistics, vol. 4. Spottiswoode, Ballantyne & Co. Ltd., London.

Bauch, C.T., Earn, D.J.D., 2003. Transients and attractors in epidemics. Proc. R. Soc. London Ser. B—Biol. Sci. 270 (1524), 1573–1578.

Bauch, C.T., Earn, D.J.D., 2004. Vaccination and the theory of games. Proc. Natl. Acad. Sci. USA 101 (36), 13391–13394.

Crawford, J.D., 1991. Introduction for bifurcation theory. Rev. Mod. Phys. 63 (4), 991–1037.

Doblhammer, G., Rodgers, J.L., Rau, R., 2000. Seasonality of birth in nineteenth- and twentieth-century Austria. Soc. Biol. 47 (3–4), 201–217.

Dushoff, J., Huang, W.Z., Castillo-Chavez, C., 1998. Backwards bifurcations and catastrophe in simple models of fatal diseases. J. Math. Biol. 36 (3), 227–248.

Dushoff, J., Plotkin, J.B., Levin, S.A., Earn, D.J.D., 2004. Dynamical resonance can account for seasonality of influenza epidemics. Proc. Natl. Acad. Sci. USA 101 (48), 16915–16916.

Earn, D.J.D., Rohani, P., Grenfell, B.T., 1998. Persistence, chaos and synchrony in ecology and epidemiology. Proc. R. Soc. London Ser. B—Biol. Sci. 265 (1390), 7–10.

Earn, D.J.D., Rohani, P., Bolker, B.M., Grenfell, B.T., 2000. A simple model for complex dynamical transitions in epidemics. Science 287 (5453), 667–670.

Earn, D.J.D., Dushoff, J., Levin, S.A., 2002. Ecology and evolution of the flu. Trends Ecol. Evol. 17 (7), 334–340.

Fine, P.E.M., Clarkson, J.A., 1982. Measles in England and Wales—I: an analysis of factors underlying seasonal patterns. Int. J. Epidemiol. 11 (1), 5–14.

Finkenstädt, B.F., Grenfell, B.T., 2000. Time series modelling of childhood diseases: a dynamical systems approach. Appl. Stat. 49 (2), 187–205.

Glendinning, P., Perry, L.P., 1997. Melnikov analysis of chaos in a simple epidemiological model. J. Math. Biol. 35 (3), 359–373.

Greenman, J., Kamo, M., Boots, M., 2004. External forcing of ecological and epidemiological systems: a resonance approach. Physica D—Nonlinear Phenom. 190 (1–2), 136–151.

Grenfell, B., Harwood, J., 1997. (Meta)-population dynamics of infectious diseases. Trends Ecol. Evol. 12, 395–399.

Grenfell, B.T., Bjornstad, O.N., Kappey, J., 2001. Travelling waves and spatial hierarchies in measles epidemics. Nature 414 (6865), 716–723.

Guckenheimer, J., Holmes, P., 1983. Nonlinear Oscillations, Dynamical Systems, and Bifurcations of Vector Fields. Applied Mathematical Sciences, vol. 42. Springer, New York.

Haandrikman, K., 2003. Timing of births: Sunday children and summer heat. Technical Report, Population Research Centre, University of Groningen, Netherlands.

Hethcote, H.W., 2000. The mathematics of infectious diseases. SIAM Rev. 42 (4), 599–653.

Ireland, J.M., Norman, R.A., Greenman, J.V., 2004. The effect of seasonal host birth rates on population dynamics: the importance of resonance. J. Theor. Biol. 231 (2), 229–238.

Kermack, W.O., McKendrick, A.G., 1927. A contribution to the mathematical theory of epidemics. Proc. R. Soc. London Ser. A 115, 700–721.

Korobeinikov, A., Maini, P.K., 2004. A Lyapunov function and global properties for SIR and SEIR epidemiological models with nonlinear incidence. Math. Biosci. Eng. 1 (1), 57–60.

Kuznetsov, Y.A., 1995. Elements of Applied Bifurcation Theory. Applied Mathematical Sciences, third ed, vol. 112. Springer, New York.

Li, M.Y., Muldowney, J.S., 1995. Global stability for the SEIR model in epidemiology. Math. Biosci. 125 (2), 155–164.

London, W., Yorke, J.A., 1973. Recurrent outbreaks of measles, chicken pox and mumps. I. Seasonal variation in contact rates. Am. J. Epidemiol. 98 (6), 453–468.

Macki, J.W., Nistri, P., Zecca, P., 1993. Mathematical models for hysteresis. SIAM Rev. 35 (1), 94–123.

Miura, T. (Ed.), 1987. Seasonality of Birth. Progress in Biometeorology, vol. 6. SPB Academic Publishing, The Hague.

Olsen, L.F., Schaffer, W.M., 1990. Chaos versus noisy periodicity: alternative hypotheses for childhood epidemics. Science 249, 499–504.

Roberts, M.G., Kao, R.R., 1998. The dynamics of an infectious disease in a population with birth pulses. Math. Biosci. 149, 23–36.

Schenzle, D., 1984. An age-structured model of pre- and post-vaccination measles transmission. IMA J. Math. Appl. Med. Biol. 1, 169–191.

Schwartz, I.B., Smith, H.L., 1983. Infinite subharmonic bifurcation in an SEIR model. J. Math. Biol. 18, 233–253.

Statistics Canada, Health Statistics Division, 2006. Births (Continues: Births and Deaths). Statistics Canada Catalogue 84-210. Minister of Industry.

Trovato, F., Odynak, D., 1993. The seasonality of births in Canada and the provinces, 1881–1989: theory and analysis. Can. Stud. Popul. 20 (1), 1–41.

van den Driessche, P., Watmough, J., 2000. A simple SIS epidemic model with a backward bifurcation. J. Math. Biol. 40 (6), 525–540.

White, K.A.J., Grenfell, B.T., Hendry, R.J., Lejeune, O., Murray, J.D., 1996. Effect of seasonal host reproduction on host–macroparasite dynamics. Math. Biosci. 137 (2), 79–99.